Scattering matrix of large Saharan dust particles: Experiments and computations

O. Muñoz,[1] H. Volten,[2] J. W. Hovenier,[3] T. Nousiainen,[4] K. Muinonen,[5] D. Guirado,[1] F. Moreno,[1] and L. B. F. M. Waters[3]

Received 26 September 2006; revised 2 December 2006; accepted 1 May 2007; published 13 July 2007.

[1] We present measurements of the complete scattering matrix as a function of the scattering angle of a sample of Sahara sand particles collected from a dune in Libya. The measurements were performed at a wavelength of 632.8 nm in the scattering angle range from 4° to 174°. To facilitate the use of the experimental data for multiple-scattering calculations with polarization included, we present a synthetic scattering matrix based on the measurements and defined in the full angle range from 0° to 180°. The Libyan sample consists of large particles distributed over a narrow size distribution which makes it an interesting test case for the Ray Optics Approximation (ROA) that provides accurate results for particles with curvature radii much larger than the wavelength. Numerical simulations using the ROA are compared with the experimental data. Moreover, the traditional ROA was modified with ad hoc simple schemes of Lambertian surface elements and internal screens to study the effects of small-scale surface roughness and internal structures, respectively. Model particle shapes used in the simulations are based on a shape analysis of our sample. The traditional ray optics approximation does not reproduce the experimental data although a significant improvement is obtained if unrealistically spiky particle shapes are used. When the Lambertian schemes are applied the agreement with the experimental data improves. Still, to get a good agreement with the experimental data we need unrealistic spiky particles together with the inclusion of external Lambertian reflections. This seems to indicate that a more refined treatment is needed to reproduce the scattering effects of the small-scale surface roughness of the Libyan sand particles.

Citation: Muñoz, O., H. Volten, J. W. Hovenier, T. Nousiainen, K. Muinonen, D. Guirado, F. Moreno, and L. B. F. M. Waters (2007), Scattering matrix of large Saharan dust particles: Experiments and computations, *J. Geophys. Res.*, *112*, D13215, doi:10.1029/2006JD008074.

1. Introduction

[2] In many regions of the Earth the atmospheric aerosol component is dominated by mineral dust. Saharan dust is the main source of mineral dust over the globe [see, e.g., *Li et al.*, 1996; *Prospero and Lamb*, 2003]. Large quantities of dust are transported from sources in North Africa across the tropical Atlantic covering very large areas [*Chiapello et al.*, 2005]. Therefore Saharan dust clouds have a significant radiative impact on climate.

[3] Saharan dust particles have irregularly round shapes with small-scale surface roughness. Moreover, they are distributed over broad ranges of sizes from the submicron region up to tens of microns. All this makes it very difficult to perform a theoretical study of such type of particles. Remarkable progress in developing advanced numerical algorithms for computing electromagnetic scattering by nonspherical particles has been achieved during the last two decades [e.g., *Draine and Flatau*, 1994; *Mishchenko et al.*, 1996, 2000, 2002; *Mackowski and Mishchenko*, 1996; *Muinonen et al.*, 1996; *Yang and Liou*, 1996; *Nousiainen et al.*, 2003; *Dubovik et al.*, 2006]. Still, most analytical methods are restricted to quite simple particle geometries and their applicability is limited to certain size ranges. Consequently, experimental studies remain an important source to evaluate models used to calculate scattering properties by nonspherical particles. Moreover, the experimental data can be used as inputs of radiative transfer models.

[4] The results of many investigations seem to indicate that the majority of particles in desert dust have submicron sizes. For instance, measurements of *Levin et al.* [1980] for dust

[1]Instituto de Astrofísica de Andalucía, Consejo Superior de Investigaciones Científicas, Granada, Spain.
[2]Laboratory for Environmental Monitoring, Environment and Safety Division, National Institute of Public Health and the Environment, Bilthoven, Netherlands.
[3]Astronomical Institute "Anton Pannekoek," University of Amsterdam, Amsterdam, Netherlands.
[4]Department of Physical Sciences, University of Helsinki, Helsinki, Finland.
[5]Observatory, University of Helsinki, Helsinki, Finland.

0148-0227/07/2006JD008074

storms over the Israeli desert show a dust surface area distribution with a maximum around 2 μm. *Koren et al.* [2001] studied a set of desert dust aerosols collected on a single-stage cascade impactor on the ground during a heavy dust storm in Israel. According to these authors, more than two thirds of the studied particles have diameters smaller than 1 μm. *Falkovich et al.* [2001] studied Saharan dust samples collected over Israel, finding that 80% of the total studied particles have a projected area diameter smaller than 3.2 μm. The measurements of *Li-Jones and Prospero* [1998] and *Haywood et al.* [2001] on suspended Saharan desert dust give size distributions with median radii maxima ranging from 1.0 to 5.0 μm and even larger. In contrast, *d'Almeida and Schütz* [1983] derived desert particle sizes with maxima in a wide size range up to 100 μm and larger. Despite the fact that a high percentage of desert dust particles have a projected area diameter between 0.2 and 5 μm, a certain percentage of larger particles might be present in desert dust clouds. Since these particles contribute significantly to the overall scattering even in small quantities, it is crucial to know how to model scattering by such large particles accurately, so that the whole size distribution can be properly accounted for.

[5] As different modeling approaches with different simplifications and approximations are needed for small and large particles, it is convenient to have measurements from samples consisting only of such particles that combinations of different methods are not needed to model scattering by these samples. In this work we experimentally study the complete scattering matrix as a function of the scattering angle of a Sahara sand sample which was collected from the upper part of a dune in Libya (hereafter Libyan sand sample). Thus this sample mainly consists of large particles since small particles were blown up by the wind. The measurements were performed at 632.8 nm. The lack of experimental data at very small and very large scattering angles (0°–4° and 174°–180°) limits the direct applicability of the measured scattering matrix as a function of the scattering angle in remote sensing. Therefore we have extrapolated the experimental scattering matrix to cover the entire angle range from 0° to 180° so that it can be used for practical applications. The extrapolation of the phase function was carried out following the procedure by *Liu et al.* [2003].

[6] As mention, the Libyan sand sample consists of very large particles which makes it an ideal test case for the performance of the Ray Optics Approximation (ROA) method for natural irregularly shaped dust particles much larger than the wavelength. In this work we investigate whether a ray-optics method employing Gaussian random shapes [*Muinonen et al.*, 1996] can reproduce the experimental scattering matrix for the Libyan sand sample. Moreover, we use a modified ROA model that takes the small-scale surface roughness and internal inhomogeneities of the particles into account using heuristic ad hoc schemes [*Nousiainen et al.*, 2003]. The present study is expected to improve the accuracy of remote sensing results regarding desert surfaces. Moreover, it is relevant for the understanding of the scattering properties of asteroid surfaces presumably composed of particles large compared to the wavelength [*Muinonen et al.*, 2002].

[7] In section 2 we present a brief review of the basic scattering concepts and a description of the setup used to measure the scattering matrix of the sample. Section 3 gives a description and a discussion of the physical properties of the sample. Results of our experiments together with a "synthetic" scattering matrix, based on the measurements, are presented in sections 4 and 5. Section 6 deals with the results of the traditional and modified Ray Optics calculations together with the experimental results. The conclusions are summarized in section 7.

2. Measurement Setup

[8] The flux and state of polarization of a beam of quasi-monochromatic light can be described by means of a so-called flux vector. For a sample of randomly oriented particles separated by distances larger than their linear dimensions and in the absence of multiple scattering, the flux vectors of the incident beam, $\pi\Phi_0(\lambda)$ and scattered beam, $\pi\Phi(\lambda, \theta)$, are related by the 4×4 scattering matrix, $\mathbf{F}$, which is a function of scattering angle θ, as follows [*Van de Hulst*, 1957; *Volten et al.*, 2006]:

$$\Phi(\lambda,\theta) = \frac{\lambda^2}{4\pi^2 D^2} \begin{pmatrix} F_{11} & F_{12} & F_{13} & F_{14} \\ F_{12} & F_{22} & F_{23} & F_{24} \\ -F_{13} & -F_{23} & F_{33} & F_{34} \\ F_{14} & F_{24} & -F_{34} & F_{44} \end{pmatrix} \Phi_0(\lambda) \quad (1)$$

where the first elements of the column vectors are fluxes divided by π and the other elements describe the state of polarization of the beams by means of Stokes parameters. Furthermore, λ is the wavelength, and D is the distance from the sample to the detector. The scattering plane, i.e., the plane containing the directions of the incident and scattered beams, is the plane of reference for the flux vectors. The matrix $\mathbf{F}$ with elements $F_{i,j}$ is called the scattering matrix. The elements of the scattering matrix are dimensionless and depend on particle properties (size, shape, and refractive index), the number of the scattering particles that contribute to the detected radiation, the wavelength of the radiation, and the direction of the scattered light, which, for randomly oriented particles, is sufficiently described by means of the scattering angle θ.

[9] In our experimental apparatus, we use a HeNe laser (632.8 nm, 5 mW) as a light source. The scattering matrix can be determined by measuring the flux vectors of the scattered light for various flux vectors of the incident light. The laser light in our experiments passes through a polarizer and a electro-optic modulator. The modulated light is subsequently scattered by an ensemble of randomly oriented particles taken from the sample located in a jet stream produced by an aerosol generator. The scattered light may pass through a quarter-wave plate and an analyzer (both optional) and is then detected by a photomultiplier tube which moves in steps along a ring around the ensemble of particles. In this way a range of scattering angles from 4° (nearly forward scattering) to 174° (nearly backward scattering) is covered in the measurements. Owing to the lack of measurements between 0 and 4° and from 174 to 180°, we cannot measure the absolute angular dependence of the phase function. Instead, we normalize the measured phase function to 1 at 30°, i.e., the phase function is measured on a relative scale. For a detailed description of the normalization procedure see *Volten et al.* [2006]. All matrix elements (except F_{11} itself) are normalized to F_{11}, that is, we consider F_{ij}/F_{11}, with $i, j = 1$ to 4 with the

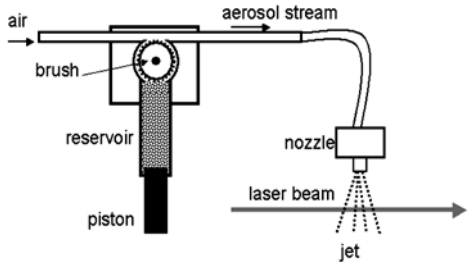

Figure 1. Schematic picture of the aerosol generator. A piston in the cylindrical feed stock reservoir pushes powder onto a rotating brush at a constant speed. An air stream carries the aerosol particles of the brush through a tube to a nozzle right above the scattering volume.

exception of $i = j = 1$. Another photomultiplier is placed at a fixed position and used to correct for fluctuations in the particle stream. Moreover, we checked that the assumption of single scattering is appropriate for our experiment [see *Hovenier et al.*, 2003]. A detailed description of the experimental apparatus used to measure the scattering matrices is given by *Hovenier* [2000].

[10] In experimental light scattering studies it is highly important to obtain well-characterized samples to be used in controlled light scattering experiments. Therefore a correct manipulation of the powder during the experiment is crucial in order to assure that the method for producing the particle jet stream does not affect the final composition, shape, and/or size distribution of the sample.

[11] To estimate whether the physical properties of the sample could be altered during measurements, let us first consider how the particles are brought into the jet stream. A compacted mass of powder is loaded into a cylindrical feed stock reservoir. A piston pushes the powder upward onto a rotating brush at a certain speed. An air stream carries the powder of the brush through a tube to a nozzle above the scattering volume. Thus the mineral particles are carried in a turbulent flow through a tube no longer than 2 meters. Therefore there is no reason to believe that a possible size/shape selection can be produced during their journey to the scattering volume. In Figure 1 we present a schematic picture of the aerosol generator.

[12] To test that the sample is not altered during the scattering measurements, firstly, we take optical and/or electron images of a representative portion of the sample that has not been through the aerosol generator. Secondly, we hold a glass plate briefly (of the order of a second) in the jet at the place where it intersects with the laser beam. When we look at the sample on the glass plate with a microscope we do not see evidence for a significant modification of the original physical properties of the sample [*Hovenier et al.*, 2003].

3. Physical Properties of the Libyan Sand Sample

3.1. Size Distributions

[13] Size is a key property in determining the light scattering properties of small particles. To describe the measured size distribution we replace each particle by a sphere with radius, r, having the same projected surface area as the particle has when averaged over all orientations. We measured the projected surface area distribution, $S(logr)$, of our Libyan sand sample using a Fritsch laser particle sizer [*Konert and Vandenberghe*, 1997] that employs a diffraction method without making any assumptions about the refractive indices of the particles. In Figure 2 we present S ($logr$) as a function of $logr$ with r in μm. $S(logr)dlogr$ is the relative contribution by projected surface equivalent spheres with radii in the size range $logr$ to $logr + dlogr$ to the total projected surface per unit volume of space.

[14] The measured $S(logr)$ can be transformed into a normalized number distributions as function of r, $n(r)$, as follows:

$$S(logr) = Cr^3 n(r) \tag{2}$$

where C is a constant which follows from the normalization condition, i.e., the integral of $n(r)$ over all particle radii must be equal to one. For more detailed information on the size distributions and on how to transform one into the other we refer to *Volten et al.* [2005] and the website http://www.astro.uva.nl/scatter.

[15] From the retrieved number distribution we obtained the values of the effective radius, r_{eff}, and effective variance, v_{eff}, defined as follows [*Hansen and Travis*, 1974]:

$$r_{\text{eff}} = \frac{\int_0^\infty r\pi r^2 n(r)dr}{\int_0^\infty \pi r^2 n(r)dr}, \tag{3}$$

$$v_{\text{eff}} = \frac{\int_0^\infty (r - r_{\text{eff}})^2 \pi r^2 n(r)dr}{r_{\text{eff}}^2 \int_0^\infty \pi r^2 n(r)dr}. \tag{4}$$

[16] The Libyan sand sample has $r_{\text{eff}} = 124.75$ μm and $v_{\text{eff}} = 0.15$. Therefore the Libyan sand sample is an interesting test case for the Ray Optics Approximation (ROA) that provides accurate results for particles with

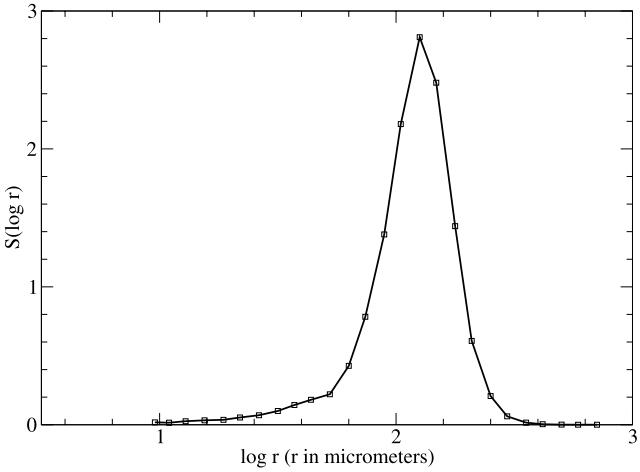

Figure 2. Measured normalized projected surface area distribution as a function of $logr$, with r expressed in micrometers.

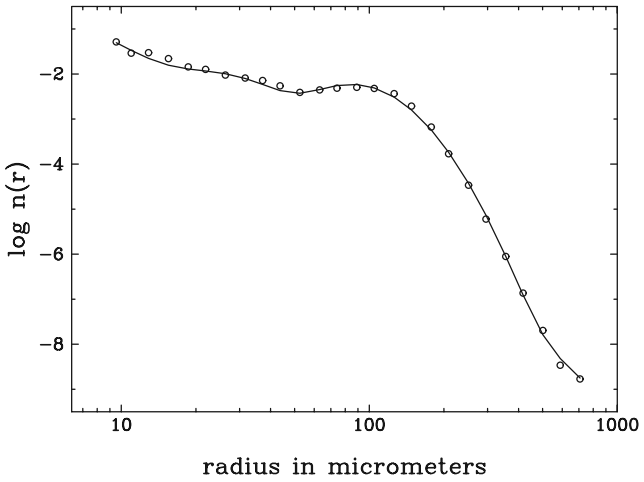

Figure 3. Fitted trimodal lognormal size distribution (solid line) and the normalized number distribution, $n(r)$ (circles), as deduced from the normalized projected surface area distribution. Number distributions for radii below about 10 micron were found to be equal to zero.

curvature radii much larger than the wavelength (see section 6.1). For modeling purposes we fitted a trimodal lognormal number distribution to the retrieved normalized number distribution, $n(r)$, of our sample as follows:

introducing

$$n_i(r) = \frac{f_i}{\sqrt{2\pi}\ln(10)\log(\sigma_i)r}\exp\left\{-\frac{[\log(r)-\log(R_i)]^2}{2\log(\sigma_i)^2}\right\}, \quad (5)$$

we write

$$n(r) = \sum_{i=1}^{3} n_i(r), \quad (6)$$

where f_i is a dimensionless parameter, σ_i the geometric standard deviation, and R_i the geometric mean radius. This type of number distribution has also been used by *d'Almeida* [1987] for desert aerosols.

[17] The fit resulted in the following parameters: f_1 = 200.63, f_2 = 0.24, f_3 = 0.45; σ_1 = 4.5, σ_2 = 1.5, and σ_3 = 1.4; R_1 = 9.0 10^{-2}, R_2 = 28.8, and R_3 = 96.5 (μm). In Figure 3 we present the retrieved normalized number distribution together with the best fit trimodal lognormal number distribution.

3.2. Shape Analysis

[18] Desert dust aerosols have a wide variety of irregular shapes. Examples of images of particles of the sample, taken with a Field Emission Scanning Electron Microscope (FESEM) and an optical microscope are shown in Figure 4. The particles in the sample have round and elongated shapes with occasional sharp edges. In Figure 4b, we show a close up of the small-scale surface structure.

[19] Several studies indicate a relation between size and shape of desert dust particles, with larger particles having sharp-edged and angular shapes [see, e.g., *Koren et al.*, 2001; *Kalashnikova and Sokolik*, 2004]. As mentioned in section 3.1, the Libyan sand sample has a very narrow projected surface area distribution. Therefore there was no need to separate it in subsamples based on their sizes to characterize the shape of its particles.

[20] A statistical shape model called the Gaussian random sphere geometry [see, e.g., *Muinonen et al.*, 1996; *Muinonen*, 2000b] was adapted to characterize the shape of the particles in the sample. The shape of a Gaussian random sphere is given by a radius vector

$$\boldsymbol{r}(\vartheta,\varphi) = \frac{a}{\sqrt{1+\sigma^2}}\exp[s(\vartheta,\varphi)]e_r, \quad (7)$$

where

$$s(\vartheta,\varphi) = \sum_{l=0}^{\infty}\sum_{m=-l}^{l} s_{lm}Y_{lm}(\vartheta,\varphi). \quad (8)$$

[21] Here ϑ and φ are spherical coordinates, a the mean radius, σ the relative standard deviation of the radius, s the so-called logradius, and $\boldsymbol{e}_r$ a unit vector pointing outward in a radial direction. The logradius is given as a real-valued series expansion of spherical harmonics Y_{lm} with degree l and order m. The complex weights s_{lm} are subject to conditions

$$s_{l,-m} = (-1)^m s_{lm}^*, \quad l = 0,1,\ldots,\infty, \quad m = -l,\ldots,-1,0,1,\ldots,l,$$

where * denotes a complex conjugate value, to keep the series expansion real-valued.

[22] Three-dimensional random shapes, i.e., individual realizations of the Gaussian random sphere geometry, are generated by randomizing the real and imaginary parts of s_{lm} which are Gaussian random variables having zero means and variances depending on the shape statistics specified by the so-called covariance function of logradius (for details, see, e.g., *Nousiainen and MacFarquhar* [2004]). To apply the Gaussian random sphere geometry for our sample particles, we needed to find the covariance function that describes the shape statistics of these particles. For this, a statistical shape analysis was performed.

[23] The shape analysis was performed exactly as in the work by *Nousiainen and MacFarquhar* [2004] for quasi-spherical ice crystals. Here, only a short overview of the analysis is given. First about a hundred sample particles were photographed with an optical microscope Olympus BX51, equipped with a digital camera with effective resolution of 2776 × 2774 pixels (Figures 4c and 4d). Then, particle silhouettes (contours separating the particles from the background) were extracted from the images. For each silhouette, the center-of-mass point was calculated to be used as an origin. Then, radius vectors specifying the silhouette with 1° angular resolution from the origin were derived. Thus sets of radius vectors were obtained, which specified each silhouette as a function of polar angle. From these radius vectors (i.e., including all silhouettes), the variance of their lengths and their (auto)correlation as a function of polar angle separating them was calculated. The latter quantity is called a correlation function of radius, and when it is multiplied by the variance of radius, the covariance function of radius is obtained. The covariance function of radius was then converted to the covariance function of

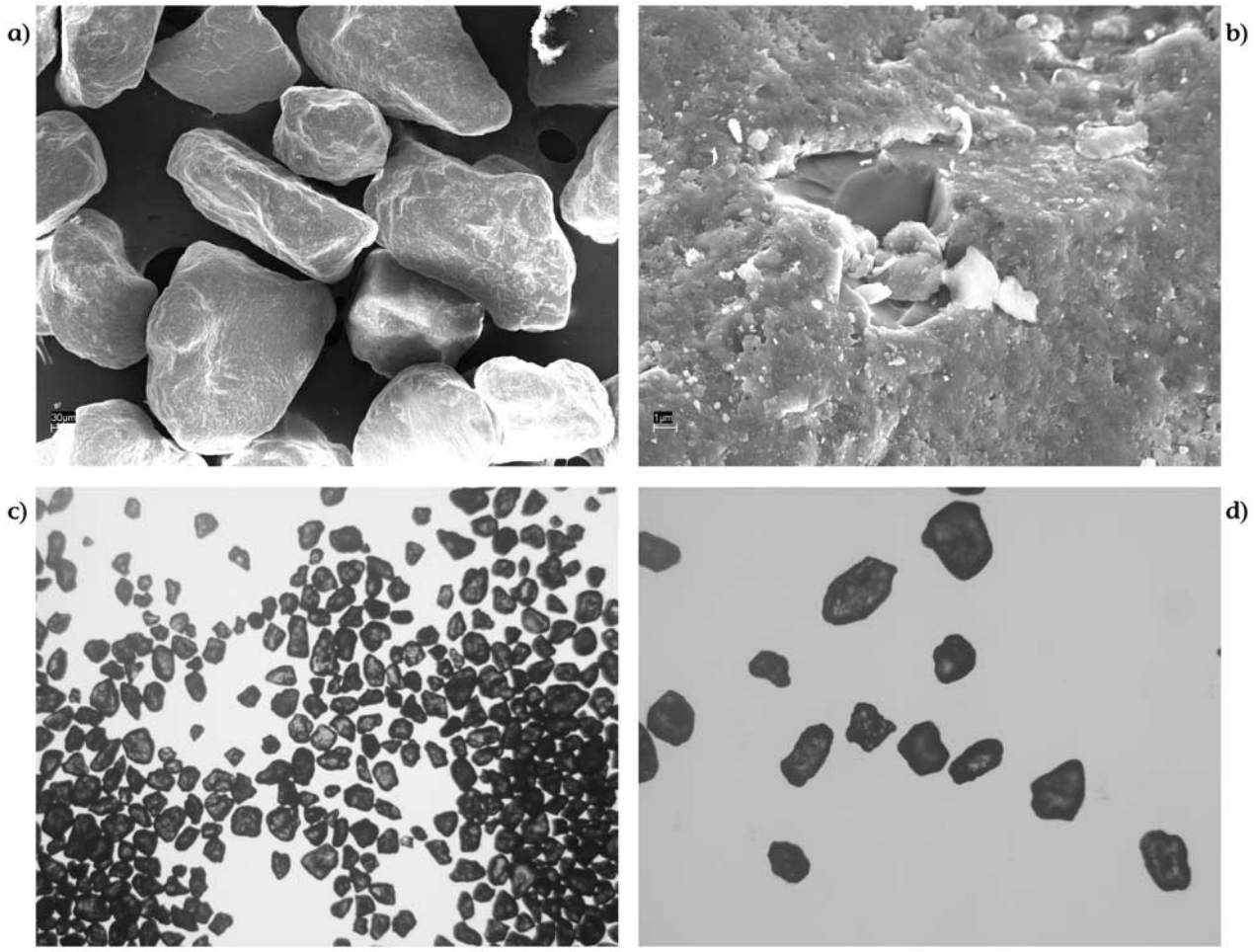

Figure 4. (a and b) FESEM and (c and d) optical microscope images of the Libyan sand sample. The white bars at the bottom left corner of Figures 4a and 4b denote 30 and 1 micron, respectively.

logradius, which specifies the statistical shape of the Gaussian random sphere and this was used as input for generating three-dimensional model particles obeying the observed shape statistics of our sample particles.

[24] The shape analysis described above assumes that the particle silhouettes are representative of random intersections of particles through the origin (unless the shape statistics are anisotropic, the radius vectors in random intersections through the origin obey the same statistics as the radius vectors in three-dimensional particles). This is not a trivial assumption, because silhouettes and random intersections through the origin are guaranteed to be identical only for perfect spheres. For random irregular shapes, they are generally different, and systematically so, because of hiding of "valleys" behind "mountains." Unfortunately, it is extremely difficult to obtain true intersections from micrometer sized particles. *Nousiainen and MacFarquhar* [2004] studied the differences of intersections and silhouettes and concluded that silhouettes underestimate the variance somewhat, but the correlation function is much less affected (except for the high-degree terms which cannot be retrieved from the silhouettes). Thus shape statistics obtained from silhouettes can be used to describe the overall shape of the particles, but information regarding possible small-scale variation is lost. One should also increase the obtained variance somewhat (10% is a good choice for typical shapes of dust particles) to compensate for the underestimation.

[25] The results of the shape analysis showed that the covariance function for our sample particles closely resemble a so-called power law covariance function. This means that if the covariance function is described by a series expansion of Legendre polynomials [see, e.g., *Muinonen*, 2000b], the weights of the Legendre polynomials (c_l) follow a power law dependence $c_l \propto l^{-\nu}$. A very similar power law dependence was found also for another sample of Saharan dust [*Nousiainen et al.*, 2003], and the same appears to be true, e.g., for the shapes of small irregular ice crystals [*Nousiainen and MacFarquhar*, 2004] and overall shapes of asteroids [*Muinonen and Lagerros*, 1998]. The shape parameters obtained for our sample were $\nu = 3.3$ and $\sigma = 0.17$. Because of the underestimation of σ when silhouettes are used, we decided to use a somewhat larger $\sigma = 0.2$ for our model particles.

[26] Finally, it is noted that in principle the series expansion, e.g., in equation (8) is infinite (the same applies to the Legendre expansion of the covariance function), but in practice the expansion can be safely truncated at some $l_{\max}$.

The sufficient l_{max} depends on the covariance function; for example if the correlation drops very rapidly with increasing angular distance, then high-degree terms are needed. The power law covariance function is special in a sense that if ν is smaller than 4.0, then the model particles are in principle fractal, which in theory means that the covariance function cannot be truncated. We tested the influence of different values of l_{max}. For $\nu = 3.3$, we varied the value of l_{max} from 25 to 75 and did not see significant differences in the calculated scattering matrices. Therefore we can assume that $l_{max} = 25$ guarantees a sufficient accuracy for the Legendre expansion of the correlation function.

3.3. Composition and Refractive Index

[27] Desert dust particles are composed of a variety of different minerals. Although the refractive indices at visible wavelengths of these constituent minerals may be known, the refractive index for the mixture may not be easy to derive from these values. *d'Almeida* [1987] attributes the different modes of the lognormal size distribution (see equations (5) and (6)) to different mineral compositions. *Patterson et al.* [1977] measured both the real, n, and imaginary, k, parts of the refractive index for different Saharan sand particles collected on three Atlantic Islands namely, Barbados, Cape Verde, and Tenerife. The measurements were performed between 300 and 700 nm. All samples studied by *Patterson et al.* [1977] present a brownish color quite similar to our Libyan sand sample. They found the values of n and k to be very similar for all studied samples assuming an average value for n equal to $n = 1.552 \pm 0.004$ at 633 nm, while the value of k varied from about 0.025 at 300 nm to approximately 0.0038 between 600 and 700 nm. *Dubovik et al.* [2002] retrieved from their aerosol radiation model a value of n in the visible part of the spectrum varying between 1.48 and 1.56 for desert dust aerosols. Other models suggest a real part of the refractive index equal to 1.53 in the same spectral region [*Shettle and Fenn*, 1979; *Koepke et al.*, 1997]. *Shettle and Fenn* [1979] obtained a value of k of 0.008 in the visible part of the spectrum whereas *Dubovik et al.* [2002] obtain values from 0.0006 to 0.003 in the same spectral region. Taking into account all these results we assume an average value $m = 1.5 + 4 \cdot 10^{-3}i$ at 632.8 nm for our Libyan sand sample.

4. Experimental Scattering Matrix

[28] In Figure 5 we present the measured scattering matrix elements as a function of the scattering angle for the Libyan sand sample. The measurements were performed at a wavelength of 632.8 nm in the scattering angle range from 4 to 174°. As mentioned in section 2, all matrix elements (except F_{11} itself) were normalized to F_{11}, that is, we consider F_{ij}/F_{11}, with $i, j = 1$ to 4 except for $i = j = 1$. The scattering functions or phase functions, $F_{11}(\theta)$, are shown on a logarithmic scale and are normalized to 1 at 30°. It follows from equation (1) that there are 10 matrix elements to be determined. This number is further reduced in case the scattering sample consists of randomly oriented particles with equal amounts of particles and their mirror particles. In that case, the four elements $F_{13}(\theta)$, $F_{14}(\theta)$, $F_{23}(\theta)$, and $F_{24}(\theta)$ are zero over their entire angle range [*Van de Hulst*, 1957, section 5.22]. As shown in Figure 5, the measured elements $F_{13}(\theta)/F_{11}(\theta)$, $F_{14}(\theta)/F_{11}(\theta)$, and $F_{24}(\theta)/F_{11}(\theta)$ are zero within the experimental errors in the complete measured scattering angle range. Because of the limited amount of sample we could not measure $F_{23}(\theta)/F_{11}(\theta)$. In any case we can assume that this ratio is also zero over the entire angle range [see *Hovenier*, 2000]. Therefore we can assume that our scattering sample consists of randomly oriented particles with equal amounts of particles and their mirror particles. Thus $-F_{12}(\theta)/F_{11}(\theta)$ is the degree of linear polarization for incident unpolarized light. We investigated the reliability of the measured scattering matrix by checking that it satisfies the Cloude test [*Hovenier and van der Mee*, 2000] within the experimental errors at each scattering angle.

[29] The measured scattering matrix elements for the Libyan sand sample follow the general trends presented by irregular mineral particles [see, e.g., *Mishchenko et al.*, 2000; *Volten et al.*, 2001]. The measured phase functions are flat functions of the scattering angle with a strong forward peak and almost no structure at side and backscattering angles. In contrast, $F_{11}(\theta)$ for spherical particles with similar refractive indices tends to increase from ~130 to ~180° [see, e.g., *Dubovik et al.*, 2001; *Mishchenko et al.*, 2002; *Herman et al.*, 2005]. We define the steepness of the $F_{11}(\theta)$ curve as the ratio of $F_{11}(5°)$ divided by the smallest value measured over the scattering angle range 5°–174°. In this way the steepness of the Libyan sand sample can be compared with the steepnesses of other studied dust samples whose $F_{11}(\theta)$ could not be measured at 4° [*Muñoz et al.*, 2000, 2001, 2002, 2004, 2006; *Volten et al.*, 2001, 2006]. The steepness of $F_{11}(\theta)$ is strongly dependent on the size of the particles since forward peaks are generally steeper for large particles than for smaller particles. However, the Libyan sand presents the highest r_{eff} of all mineral samples studied so far, but shows the smallest steepness with a value equal to 120. For instance, *Volten et al.* [2001] present experimental scattering matrices for seven distinct irregularly shaped mineral aerosol samples, namely, Feldspar, Red clay, Quartz, Loess, Pinatubo and Lokon volcanic ash, and Sahara sand. Although the latter ($r_{eff} = 8.2$ μm, $v_{eff} = 4$) differed from our Libyan sand sample, the two samples have very similar values of the steepness. Generally, the steepest phase curves occur for the smallest mineral particles. This is likely to follow from the fact that we are not taking into account measurements at scattering angles smaller than 5°. For further comparisons with different mineral samples see the Amsterdam Light Scattering Database, http://www.astro.uva.nl/scatter/.

[30] The measured degree of linear polarization for incident unpolarized light, $-F_{12}(\theta)/F_{11}(\theta)$, shows the typical bell shape presented by irregular mineral particles with a maximum of 16% at 90°. The measured $F_{34}(\theta)/F_{11}(\theta)$ presents values close to zero at all measured scattering angles ranging from 0.05 at 80° to −0.0003 at 4°.

[31] For homogeneous, optically inactive spheres, the $F_{22}(\theta)/F_{11}(\theta)$ and $F_{33}(\theta)/F_{44}(\theta)$ ratios are equal to unity at all scattering angles. As shown in Figure 5 (middle), the $F_{22}(\theta)/F_{11}(\theta)$ decreases smoothly from close to unity in the forward direction to a minimum at side scattering angles increasing again toward back scattering. Moreover, as shown in Figure 6, the measured $F_{33}(\theta)/F_{11}(\theta)$ is larger than $F_{44}(\theta)/F_{11}(\theta)$ in the scattering angle ranges from 4 to 75° and from

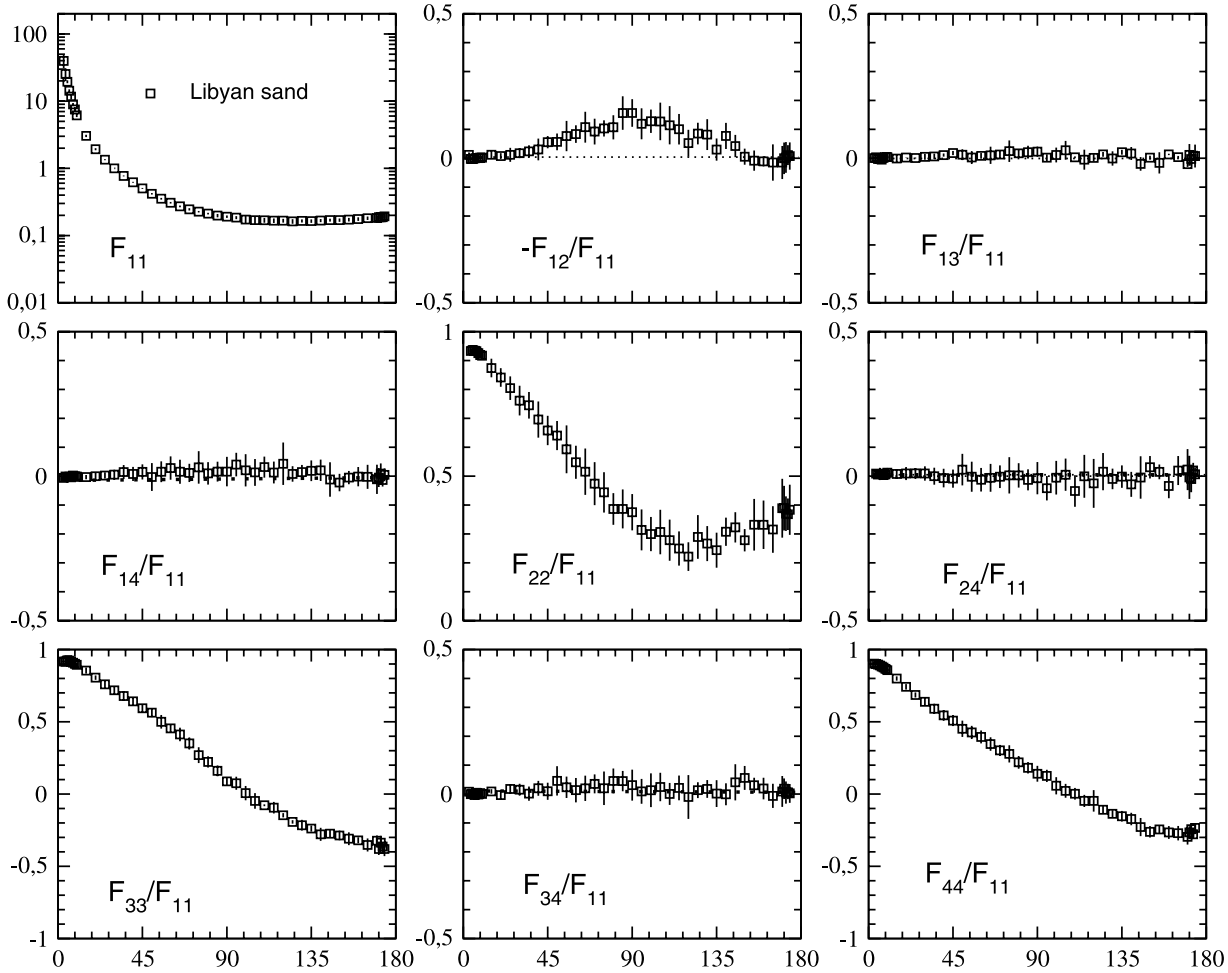

Figure 5. Measured scattering matrix elements as functions of the scattering angle at 632.8 nm for the Libyan sand sample. Error are indicated by error bars or are within the symbols.

105 to 174°. Therefore the measured values for the ratios $F_{22}(\theta)/F_{11}(\theta)$ and $F_{33}(\theta)/F_{44}(\theta)$, indicate the nonsphericity of our Libyan sand particles.

5. Synthetic Scattering Matrix for the Libyan Sand

[32] As mentioned, the measurements do not cover either the exact forward or the exact backward scattering direction. Therefore what we obtain is the relative phase function, $F_{11}(\theta)/F_{11}(30°)$, where [see *Volten et al.*, 2006],

$$\frac{F_{11}(\theta)}{F_{11}(30^\circ)} = \frac{F_{11}^{au}(\theta)}{F_{11}^{au}(30^\circ)} \tag{9}$$

in which $F_{11}^{au}(\theta)$ is the phase function, normalized so that its average over all directions equals unity, i.e.,

$$\frac{1}{2}\int_o^\pi d\theta \sin\theta F_{11}^{au}(\theta) = 1 \tag{10}$$

The lack of measurements in forward and backward directions limits the use of the measured scattering matrix data for radiative transfer calculations. To facilitate the use of the measurements for multiple scattering calculations, we constructed a synthetic scattering matrix from our measurements. The synthetic scattering matrix is defined in the full

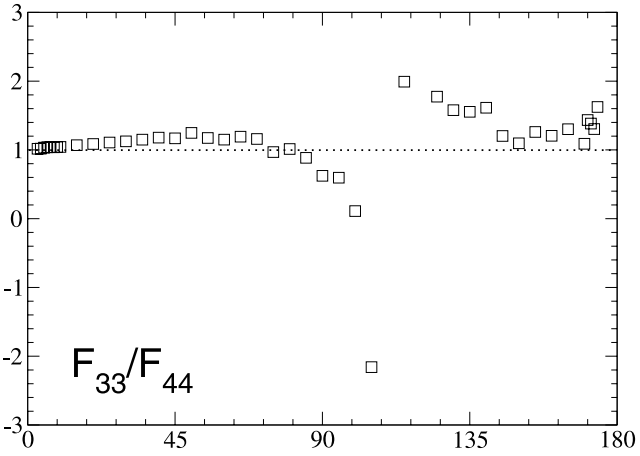

Figure 6. Measured F_{33}/F_{44} ratios as functions of the scattering angle at 632.8 nm for the Libyan sand sample.

Table 1. Synthetic Scattering Matrix Elements, $F_{i,j}^{au}$, as Functions of the Scattering Angle for the Libyan Sand Sample at 632.8 nm[a]

Angle, deg	F_{11}^{au}	$-F_{12}^{au}/F_{11}^{au}$	F_{22}^{au}/F_{11}^{au}	F_{33}^{au}/F_{11}^{au}	F_{34}^{au}/F_{11}^{au}	F_{44}^{au}/F_{11}^{au}	$\overline{F_{11}}$
0	$2.16 \cdot 10^{6}$	$0.00 \cdot 10^{0}$	$9.19 \cdot 10^{-1}$	$9.19 \cdot 10^{-1}$	$0.00 \cdot 10^{0}$	$9.17 \cdot 10^{-1}$	–
1	$3.63 \cdot 10^{2}$	$-4.96 \cdot 10^{-4}$	$9.23 \cdot 10^{-1}$	$9.17 \cdot 10^{-1}$	$-6.46 \cdot 10^{-4}$	$9.13 \cdot 10^{-1}$	–
2	$5.21 \cdot 10^{1}$	$-9.37 \cdot 10^{-4}$	$9.26 \cdot 10^{-1}$	$9.14 \cdot 10^{-1}$	$-1.68 \cdot 10^{-3}$	$9.09 \cdot 10^{-1}$	–
3	$1.60 \cdot 10^{1}$	$-1.49 \cdot 10^{-3}$	$9.29 \cdot 10^{-1}$	$9.12 \cdot 10^{-1}$	$-1.94 \cdot 10^{-3}$	$9.05 \cdot 10^{-1}$	–
4	$7.47 \cdot 10^{0}$	$-2.31 \cdot 10^{-3}$	$9.33 \cdot 10^{-1}$	$9.17 \cdot 10^{-1}$	$-2.86 \cdot 10^{-4}$	$9.00 \cdot 10^{-1}$	$7.32 \cdot 10^{0}$
5	$5.59 \cdot 10^{0}$	$-2.76 \cdot 10^{-3}$	$9.36 \cdot 10^{-1}$	$9.26 \cdot 10^{-1}$	$9.99 \cdot 10^{-5}$	$8.96 \cdot 10^{-1}$	$5.59 \cdot 10^{0}$
10	$1.77 \cdot 10^{0}$	$2.13 \cdot 10^{-2}$	$9.17 \cdot 10^{-1}$	$8.94 \cdot 10^{-1}$	$4.91 \cdot 10^{-3}$	$8.57 \cdot 10^{-1}$	$1.77 \cdot 10^{0}$
15	$8.76 \cdot 10^{-1}$	$1.19 \cdot 10^{-2}$	$8.74 \cdot 10^{-1}$	$8.54 \cdot 10^{-1}$	$9.03 \cdot 10^{-3}$	$7.99 \cdot 10^{-1}$	$8.76 \cdot 10^{-1}$
20	$5.54 \cdot 10^{-1}$	$7.53 \cdot 10^{-3}$	$8.41 \cdot 10^{-1}$	$8.06 \cdot 10^{-1}$	$-3.58 \cdot 10^{-3}$	$7.42 \cdot 10^{-1}$	$5.53 \cdot 10^{-1}$
25	$3.87 \cdot 10^{-1}$	$1.18 \cdot 10^{-2}$	$8.05 \cdot 10^{-1}$	$7.59 \cdot 10^{-1}$	$1.75 \cdot 10^{-2}$	$6.86 \cdot 10^{-1}$	$3.86 \cdot 10^{-1}$
30	$2.88 \cdot 10^{-1}$	$1.74 \cdot 10^{-2}$	$7.61 \cdot 10^{-1}$	$7.18 \cdot 10^{-1}$	$1.51 \cdot 10^{-2}$	$6.39 \cdot 10^{-1}$	$2.88 \cdot 10^{-1}$
35	$2.22 \cdot 10^{-1}$	$2.38 \cdot 10^{-2}$	$7.45 \cdot 10^{-1}$	$6.78 \cdot 10^{-1}$	$1.46 \cdot 10^{-3}$	$5.90 \cdot 10^{-1}$	$2.22 \cdot 10^{-1}$
40	$1.79 \cdot 10^{-1}$	$3.05 \cdot 10^{-2}$	$6.96 \cdot 10^{-1}$	$6.41 \cdot 10^{-1}$	$1.99 \cdot 10^{-2}$	$5.44 \cdot 10^{-1}$	$1.79 \cdot 10^{-1}$
45	$1.45 \cdot 10^{-1}$	$5.56 \cdot 10^{-2}$	$6.58 \cdot 10^{-1}$	$5.94 \cdot 10^{-1}$	$9.62 \cdot 10^{-3}$	$5.08 \cdot 10^{-1}$	$1.45 \cdot 10^{-1}$
50	$1.20 \cdot 10^{-1}$	$5.67 \cdot 10^{-2}$	$6.40 \cdot 10^{-1}$	$5.63 \cdot 10^{-1}$	$4.57 \cdot 10^{-2}$	$4.52 \cdot 10^{-1}$	$1.20 \cdot 10^{-1}$
55	$1.02 \cdot 10^{-1}$	$7.69 \cdot 10^{-2}$	$5.93 \cdot 10^{-1}$	$5.00 \cdot 10^{-1}$	$2.34 \cdot 10^{-2}$	$4.26 \cdot 10^{-1}$	$1.02 \cdot 10^{-1}$
60	$8.85 \cdot 10^{-2}$	$8.36 \cdot 10^{-2}$	$5.48 \cdot 10^{-2}$	$4.55 \cdot 10^{-1}$	$1.35 \cdot 10^{-2}$	$3.95 \cdot 10^{-1}$	$8.84 \cdot 10^{-2}$
65	$7.82 \cdot 10^{-2}$	$1.08 \cdot 10^{-1}$	$5.15 \cdot 10^{-1}$	$4.12 \cdot 10^{-1}$	$1.98 \cdot 10^{-2}$	$3.46 \cdot 10^{-1}$	$7.83 \cdot 10^{-2}$
70	$7.06 \cdot 10^{-2}$	$9.24 \cdot 10^{-2}$	$4.74 \cdot 10^{-1}$	$3.50 \cdot 10^{-1}$	$3.30 \cdot 10^{-1}$	$3.02 \cdot 10^{-1}$	$7.06 \cdot 10^{-2}$
75	$6.52 \cdot 10^{-2}$	$1.03 \cdot 10^{-1}$	$4.44 \cdot 10^{-1}$	$2.69 \cdot 10^{-1}$	$2.00 \cdot 10^{-2}$	$2.78 \cdot 10^{-1}$	$6.54 \cdot 10^{-2}$
80	$6.10 \cdot 10^{-2}$	$1.07 \cdot 10^{-1}$	$3.86 \cdot 10^{-1}$	$2.22 \cdot 10^{-1}$	$4.53 \cdot 10^{-2}$	$2.20 \cdot 10^{-1}$	$6.11 \cdot 10^{-2}$
85	$5.71 \cdot 10^{-2}$	$1.56 \cdot 10^{-1}$	$3.87 \cdot 10^{-1}$	$1.61 \cdot 10^{-1}$	$4.48 \cdot 10^{-2}$	$1.82 \cdot 10^{-1}$	$5.70 \cdot 10^{-2}$
90	$5.49 \cdot 10^{-2}$	$1.57 \cdot 10^{-1}$	$3.75 \cdot 10^{-1}$	$8.75 \cdot 10^{-2}$	$3.08 \cdot 10^{-2}$	$1.40 \cdot 10^{-1}$	$5.50 \cdot 10^{-2}$
95	$5.32 \cdot 10^{-2}$	$1.19 \cdot 10^{-1}$	$3.11 \cdot 10^{-1}$	$7.48 \cdot 10^{-2}$	$9.31 \cdot 10^{-3}$	$1.25 \cdot 10^{-1}$	$5.32 \cdot 10^{-2}$
100	$4.98 \cdot 10^{-2}$	$1.28 \cdot 10^{-1}$	$3.00 \cdot 10^{-1}$	$6.34 \cdot 10^{-3}$	$1.32 \cdot 10^{-2}$	$5.74 \cdot 10^{-2}$	$4.98 \cdot 10^{-2}$
105	$4.88 \cdot 10^{-2}$	$1.33 \cdot 10^{-1}$	$3.07 \cdot 10^{-1}$	$-4.77 \cdot 10^{-2}$	$2.44 \cdot 10^{-2}$	$2.21 \cdot 10^{-2}$	$4.90 \cdot 10^{-2}$
110	$4.86 \cdot 10^{-2}$	$1.14 \cdot 10^{-1}$	$2.78 \cdot 10^{-1}$	$-7.75 \cdot 10^{-2}$	$4.02 \cdot 10^{-4}$	$1.99 \cdot 10^{-3}$	$4.87 \cdot 10^{-2}$
115	$4.80 \cdot 10^{-2}$	$1.00 \cdot 10^{-1}$	$2.49 \cdot 10^{-1}$	$-9.45 \cdot 10^{-2}$	$2.12 \cdot 10^{-2}$	$-4.74 \cdot 10^{-2}$	$4.81 \cdot 10^{-2}$
120	$4.79 \cdot 10^{-2}$	$5.23 \cdot 10^{-2}$	$2.22 \cdot 10^{-1}$	$-1.47 \cdot 10^{-1}$	$-1.02 \cdot 10^{-2}$	$-4.74 \cdot 10^{-2}$	$4.78 \cdot 10^{-2}$
125	$4.67 \cdot 10^{-2}$	$8.53 \cdot 10^{-2}$	$2.90 \cdot 10^{-1}$	$-1.93 \cdot 10^{-1}$	$1.34 \cdot 10^{-2}$	$-1.09 \cdot 10^{-1}$	$4.67 \cdot 10^{-2}$
130	$4.76 \cdot 10^{-2}$	$8.18 \cdot 10^{-2}$	$2.67 \cdot 10^{-1}$	$-2.16 \cdot 10^{-1}$	$1.75 \cdot 10^{-2}$	$-1.37 \cdot 10^{-1}$	$4.75 \cdot 10^{-2}$
135	$4.73 \cdot 10^{-2}$	$3.00 \cdot 10^{-2}$	$2.44 \cdot 10^{-1}$	$-2.39 \cdot 10^{-1}$	$1.64 \cdot 10^{-3}$	$-1.54 \cdot 10^{-1}$	$4.72 \cdot 10^{-2}$
140	$4.81 \cdot 10^{-2}$	$7.73 \cdot 10^{-2}$	$3.08 \cdot 10^{-1}$	$-2.79 \cdot 10^{-1}$	$-8.16 \cdot 10^{-4}$	$-1.73 \cdot 10^{-1}$	$4.81 \cdot 10^{-2}$
145	$4.89 \cdot 10^{-2}$	$4.22 \cdot 10^{-2}$	$3.23 \cdot 10^{-1}$	$-2.75 \cdot 10^{-1}$	$4.01 \cdot 10^{-2}$	$-2.28 \cdot 10^{-1}$	$4.90 \cdot 10^{-2}$
150	$4.89 \cdot 10^{-2}$	$5.27 \cdot 10^{-3}$	$2.78 \cdot 10^{-1}$	$-2.87 \cdot 10^{-1}$	$5.58 \cdot 10^{-2}$	$-2.61 \cdot 10^{-1}$	$4.90 \cdot 10^{-2}$
155	$4.97 \cdot 10^{-2}$	$-8.32 \cdot 10^{-3}$	$3.32 \cdot 10^{-1}$	$-3.09 \cdot 10^{-1}$	$3.04 \cdot 10^{-2}$	$-2.45 \cdot 10^{-1}$	$4.98 \cdot 10^{-2}$
160	$5.06 \cdot 10^{-2}$	$-1.08 \cdot 10^{-2}$	$3.32 \cdot 10^{-1}$	$-3.20 \cdot 10^{-1}$	$1.91 \cdot 10^{-2}$	$-2.66 \cdot 10^{-1}$	$5.07 \cdot 10^{-2}$
165	$5.22 \cdot 10^{-2}$	$-1.49 \cdot 10^{-2}$	$3.15 \cdot 10^{-1}$	$-3.52 \cdot 10^{-1}$	$-6.32 \cdot 10^{-3}$	$-2.71 \cdot 10^{-1}$	$5.21 \cdot 10^{-2}$
170	$5.26 \cdot 10^{-2}$	$-1.49 \cdot 10^{-2}$	$3.89 \cdot 10^{-1}$	$-3.23 \cdot 10^{-1}$	$8.89 \cdot 10^{-3}$	$-2.96 \cdot 10^{-1}$	$5.27 \cdot 10^{-2}$
171	$5.40 \cdot 10^{-2}$	$-7.60 \cdot 10^{-5}$	$3.89 \cdot 10^{-1}$	$-3.80 \cdot 10^{-1}$	$1.84 \cdot 10^{-2}$	$-2.65 \cdot 10^{-1}$	$5.41 \cdot 10^{-2}$
172	$5.37 \cdot 10^{-2}$	$2.89 \cdot 10^{-3}$	$3.70 \cdot 10^{-1}$	$-3.36 \cdot 10^{-1}$	$5.18 \cdot 10^{-3}$	$-2.43 \cdot 10^{-1}$	$5.39 \cdot 10^{-2}$
173	$5.40 \cdot 10^{-2}$	$1.08 \cdot 10^{-2}$	$3.68 \cdot 10^{-1}$	$-3.63 \cdot 10^{-1}$	$6.02 \cdot 10^{-3}$	$-2.79 \cdot 10^{-1}$	$5.41 \cdot 10^{-2}$
174	$5.55 \cdot 10^{-2}$	$7.43 \cdot 10^{-3}$	$3.84 \cdot 10^{-1}$	$-3.80 \cdot 10^{-1}$	$2.33 \cdot 10^{-3}$	$-2.34 \cdot 10^{-1}$	$5.56 \cdot 10^{-2}$
175	$5.72 \cdot 10^{-2}$	$2.82 \cdot 10^{-3}$	$4.01 \cdot 10^{-1}$	$-3.91 \cdot 10^{-1}$	$-1.51 \cdot 10^{-3}$	$-1.74 \cdot 10^{-1}$	–
176	$5.88 \cdot 10^{-2}$	$6.43 \cdot 10^{-4}$	$4.17 \cdot 10^{-1}$	$-4.06 \cdot 10^{-1}$	$-2.87 \cdot 10^{-3}$	$-1.23 \cdot 10^{-1}$	–
177	$6.03 \cdot 10^{-2}$	$7.86 \cdot 10^{-5}$	$4.32 \cdot 10^{-1}$	$-4.23 \cdot 10^{-1}$	$-2.56 \cdot 10^{-3}$	$-7.92 \cdot 10^{-2}$	–
178	$6.18 \cdot 10^{-2}$	$3.22 \cdot 10^{-4}$	$4.47 \cdot 10^{-1}$	$-4.41 \cdot 10^{-1}$	$-1.43 \cdot 10^{-3}$	$-3.81 \cdot 10^{-2}$	–
179	$6.33 \cdot 10^{-2}$	$5.65 \cdot 10^{-4}$	$4.61 \cdot 10^{-1}$	$-4.59 \cdot 10^{-1}$	$-3.02 \cdot 10^{-4}$	$2.86 \cdot 10^{-3}$	–
180	$6.48 \cdot 10^{-2}$	$0.00 \cdot 10^{0}$	$4.76 \cdot 10^{-1}$	$-4.76 \cdot 10^{-1}$	$0.00 \cdot 10^{0}$	$4.71 \cdot 10^{-2}$	–

[a]Also shown (last column) is the renormalized measured phase function, $\overline{F_{11}}$.

range from 0 to 180°. For the extension of the phase function, we followed the procedure described by *Liu et al.* [2003], which is based on the assumption that the forward scattering peak for randomly oriented particles with moderate aspect ratios mainly depends on the size of the particles [*Mishchenko et al.*, 1996, 1997]. Thus we scaled the measured phase function until its value at 4° matched the Lorenz-Mie calculations for projected surface area equivalent spheres. For the Lorenz-Mie calculations we used the measured size distribution for our sand sample assuming a refractive index equal to $m = 1.5 + 4 \cdot 10^{-3} i$ (see section 3.3). The scaled phase function was then extrapolated to 180° assuming a smooth polynomial extrapolation. Once the scattering function is defined in the full range from 0 to 180°, we checked whether the normalization condition (equation (10)) was satisfied. Since this condition was not satisfied, the measured point at the overlap angle (in this case 4°) was iteratively adjusted until the normalization condition was satisfied.

[33] For the relative scattering matrix elements F_{ij}/F_{11} with (i, j = 1 to 4 with the exception of $i = j = 1$), a polynomial extrapolation was used for both the forward and the backscattering direction. Values at exact forward and backward scattering were determined so that they satisfy the conditions given by *Hovenier et al.* [2004, section 2.7].

$$F_{12}(\theta)/F_{11}(\theta) = F_{34}(\theta)/F_{11}(\theta) = 0 (\theta = 0^\circ, 180^\circ) \tag{11}$$

$$F_{22}(0^\circ)/F_{11}(0^\circ) = F_{33}(0^\circ)/F_{11}(0^\circ) \tag{12}$$

$$1 \geq |F_{22}(0^\circ)/F_{11}(0^\circ)| \tag{13}$$

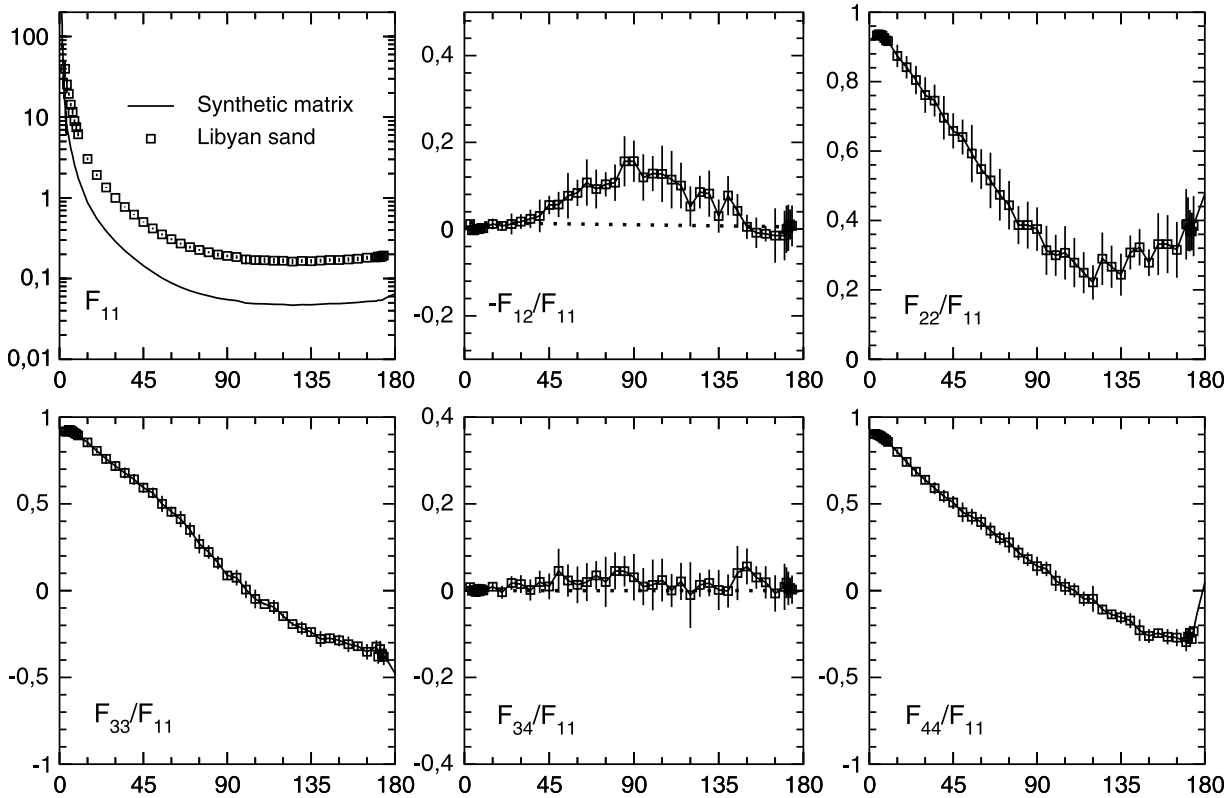

Figure 7. Measured scattering matrix elements as functions of the scattering angle at 632.8 nm for the Libyan sand sample (squares). Solid lines correspond to the synthetic scattering matrix elements. Note that $F_{11}(\theta)$ (squares) is normalized to 1 at 30° whereas $F_{11}^{au}(\theta)$ (solid line, top left corner) is normalized so that its average over all directions equals unity.

$$1 \geq |F_{44}(0^\circ)/F_{11}(0^\circ)| \tag{14}$$

$$F_{44}(0^\circ)/F_{11}(0^\circ) \geq 2|F_{22}(0^\circ)/F_{11}(0^\circ)| - 1 \tag{15}$$

$$F_{22}(180^\circ)/F_{11}(180^\circ) = -F_{33}(180^\circ)/F_{11}(180^\circ) \tag{16}$$

$$1 \geq |F_{22}(180^\circ)/F_{11}(180^\circ)| \geq 0 \tag{17}$$

$$F_{44}(180^\circ)/F_{11}(180^\circ) = 1 - 2F_{22}(180^\circ)/F_{11}(180^\circ). \tag{18}$$

[34] The resulting synthetic scattering matrix for Libyan sand satisfies the Cloude (coherency matrix) test at all scattering angles as described by *Hovenier and van der Mee* [2000]. The resulting fits are presented in Figure 7. In Table 1, we present the values of the synthetic scattering matrix for the Libyan sand sample, together with the values of the renormalized measured phase function, $\overline{F_{11}}(\theta)$, i.e., the measured phase function renormalized so that its value at 30° is the same as that of $F_{11}^{au}(\theta)$. It should be noted that $F_{i,j}(\theta)/F_{11}(\theta) = F_{i,j}^{au}(\theta)/F_{11}^{au}(\theta)$ for all values i, j = 1, 2, 3, 4.

6. Computations

[35] In section 6.1, we give a description of the light-scattering model used to analyze the measured scattering matrix elements for the Libyan sand sample. A sensitivity study for the traditional Ray Optics Approximation, ROA, method is presented in section 6.2.1. In section 6.2.2 we describe the sensitivity tests for the ROA method including the Lambertian schemes.

6.1. Ray Optics Method

[36] In the Ray Optics Approximation (ROA), the total amount of light scattered by a particle is the sum of diffracted, reflected and transmitted components [see, e.g., *Bohren and Huffman*, 1983, section 4.7]. Strictly speaking, the ROA is valid when the curvature of the particle surface is much larger than the wavelength of the incident radiation everywhere on the particle and the surface can thus be considered locally plane, and when the phase differences between internal and external fields across the surface irregularities are sufficiently large to suppress the interference effects associated with the irregularities [*Muinonen et al.*, 1997]. The conditions can be summarized, respectively, by the following inequalities: $x_c \gg 1$ and $2x_c\,|m-1| \gg 1$, where $x_c = 2\pi r_c/\lambda$ is the curvature size parameter, r_c is the curvature radius, and m the complex refractive index. However, the ROA may provide sufficiently accurate results even when these conditions are not well met, and it is often preferable to use the ROA somewhat beyond its validity region rather than using the alternative methods, which usually cannot account for irregular particle shapes. It is noted that the lower particle size limit the ROA can be applied to is not well defined and difficult to establish as it

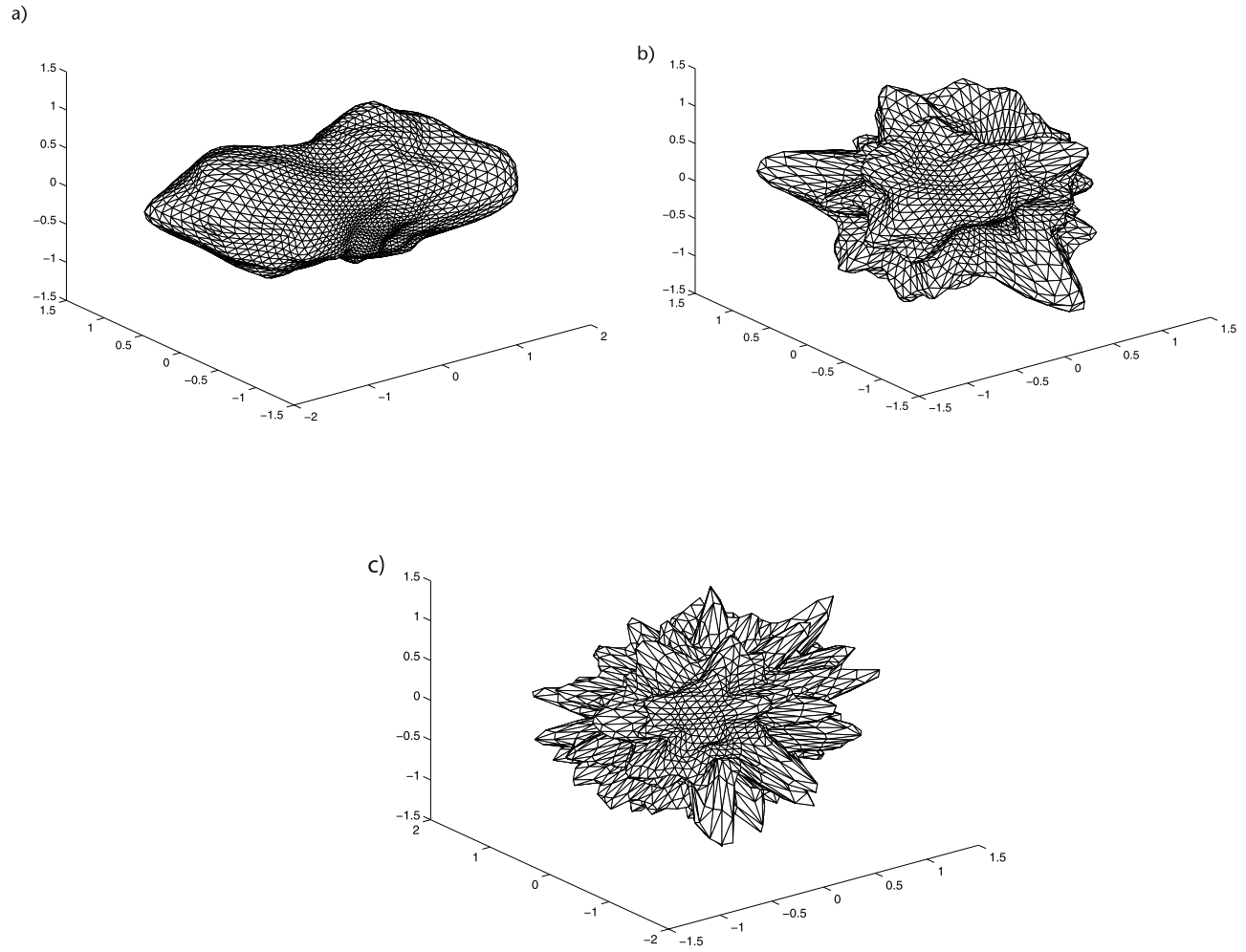

Figure 8. Images of model particles using a power law correlation function with $\nu = 3.3$, $\sigma = 2$, and (a) $l_{min} = 2$, (b) $l_{min} = 5$, and (c) $l_{min} = 10$.

depends, for example, on particle shape and composition. However, our Libyan sand sample consists of large particles with overall curvature radii much larger than the wavelength but the particles are partly covered with wavelength-scale surface roughness. It is interesting to study the performance of ROA on these particles and to disentangle the potential effects from surface roughness.

[37] The ROA model used consists of two parts, one accounting for diffraction and the other for the transmitted and reflected radiation by means of geometric optics. The solution for diffraction is based on the Kirchhoff approximation for equivalent projected surface area spheres, i.e., the solution is insensitive to particle shape and composition. The model used is the same as that used by *Nousiainen et al.* [2003] for a different sample of Sahara sand particles included in the Amsterdam Light Scattering Database (see also section 4). In that case, the sample had a relatively high percentage of small particles having a r_{eff} and v_{eff} equal to 8.2 μm and 4.0, respectively.

[38] The geometric optics part is solved using the Monte Carlo ray-tracing technique. The model is a discretized version of the model explained thoroughly by *Muinonen et al.* [1996]. The discretization means that the particle is defined as a wire frame of triangles instead of a continuous function [see *Muinonen*, 2000a]. When sufficiently small triangles are used, the solution converges to the solution for a continuous surface, and the discretization allows for solving the contact points of light rays and the particle surface analytically.

[39] In traditional geometric optics, planar surfaces are thought to reflect and transmit light on the basis of the law of specular reflection and the so-called Snel's law. We call such a model Fresnelian geometric optics. If the particle surface is smooth (e.g., optical lenses, liquid droplets), such an approach works well. If, on the other hand, there is roughness at the wavelength-scale on the surface, such roughness cannot be accounted for by using small enough triangles, the surface elements would be too small for the assumptions of the ROA and the surface could not assumed to be locally plane. Such a surface scatters light rather diffusively. Strictly speaking, such a surface cannot be modeled using geometric optics. However, there is no method available today that could handle particles much larger than the wavelength with surface features at the scale of the wavelength in a physically rigorous way. It is therefore reasonable to test how the ROA method would perform if its geometric optics

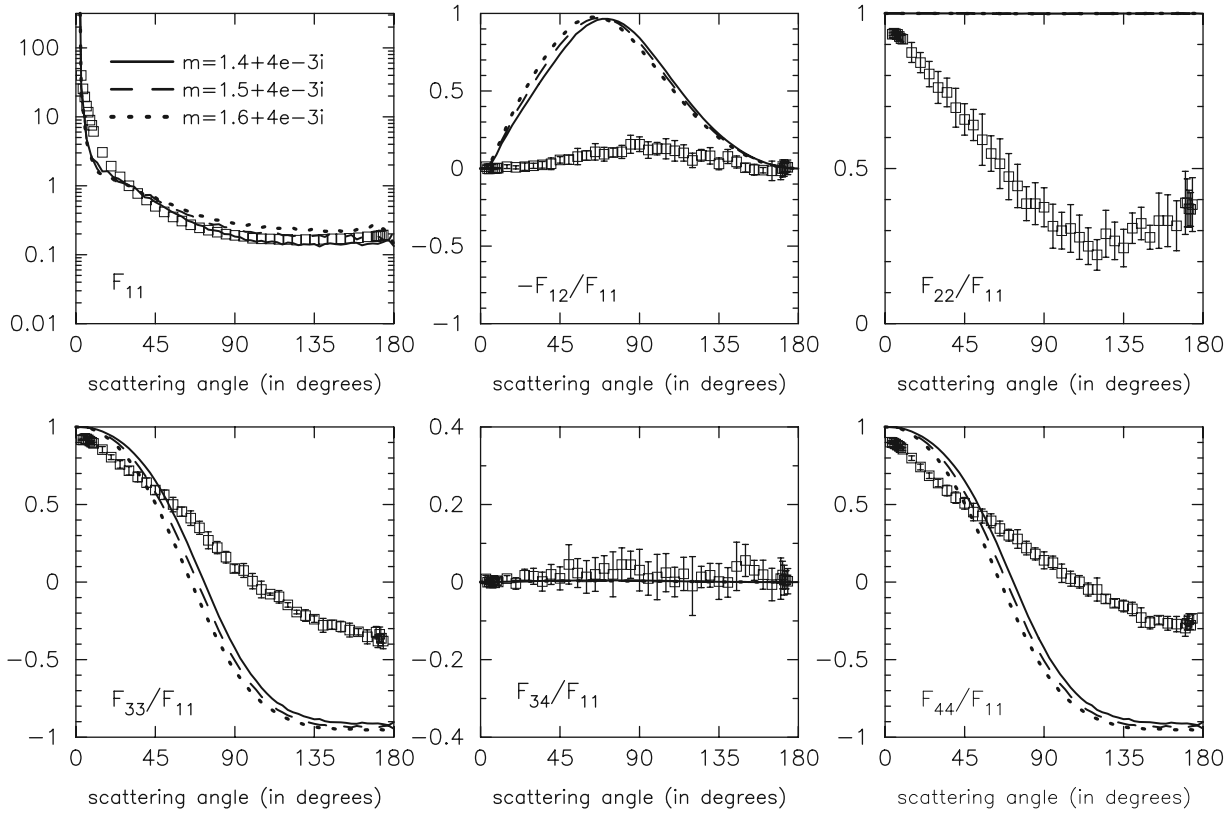

Figure 9. Scattering matrix elements computed with the traditional ray-optics method. The real part of the refractive index, n is varied from 1.4 to 1.6. Further, we used $l_{min} = 2$, $\sigma = 0.2$, and the imaginary part of the refractive index, k, equal to 4E-3. The calculations are presented together with the experimental scattering matrix for Libyan sand at 632.8 nm (squares). Errors are indicated by error bars or are within the symbols.

part was modified to approximately account for such a surface in its reflection and transmission laws.

[40] To account for the effect of small-scale roughness on scattering approximately, our ROA model has been modified by introducing an alternative scattering law for reflection and transmission. Further, a scheme for internal inhomogeneity is added. These modifications are described by *Nousiainen et al.* [2003]. The general assumption is that the small-scale surface roughness makes scattering more diffuse, and this is accomplished by allowing some scattering events to be Lambertian rather than Fresnelian. The interaction with Lambertian elements differs from the interaction with normal (Fresnelian elements) in that, instead of multiplying the rays with Fresnelian reflection and transmission matrices [*Muinonen et al.*, 1996], and obtaining the reflection angle from the law of specular reflection and transmission angle from Snel's law, the rays are multiplied by Lambertian reflection/transmission matrices and the new direction for the rays are obtained from the Lambertian scattering law; $\theta' = \arccos(\sqrt{\xi_1})$, $\phi' = 2\pi\xi_2$, where the angles θ' and ϕ' specify the zenith and azimuth angles with respect to the scattering element and ξ is a random number uniformly distributed between 0 and 1. The Lambertian reflection/transmission matrix has a diagonal form diag(1, 0, 0, 0), i.e., rays are fully depolarized [see, e.g., *Hovenier et al.*, 2004, section 5.6]. In the work by *Nousiainen et al.* [2003], two different forms (linearly depolarizing and fully depolarizing) were considered, but the former leads to quite unrealistic values for the F_{44} matrix element and is not considered here. It is noted that the Lambertian reflection/transmission matrix is not based on measurements but is a simple ad hoc generalization for diffuse reflection/transmission.

[41] The probability between Fresnelian and Lambertian interaction depends on the surface area fraction f_{ex} of Lambertian surface elements, which is a free parameter. Similarly to the surface roughness, we have a Lambertian scheme for the internal structure, in which an internal ray has a possibility to hit randomly oriented Lambertian screens inside the particle, the probability depending on the mean free path length δ_{in} inside the particle (probability = $1 - \exp(-\text{path length}/\delta_{in})$). As δ_{in} characterizes a material, not a particle, it is independent of particle size. Both the Lambertian surface elements and internal screens also have a given plane albedo, α_{ex} and α_{in}, respectively, which are also free parameters.

[42] As mentioned in section 3.2, the model particles are generated according to a statistical method based on the Gaussian random sphere [see, e.g., *Muinonen et al.*, 1996; *Muinonen*, 2000b]. In our case, the shape of the model particles depends on the shape parameters ν and σ, which were derived from the shape analysis of the micrographs of the sample particles. Further, we need to define the extent of the spherical harmonics expansion in equation (8) for the

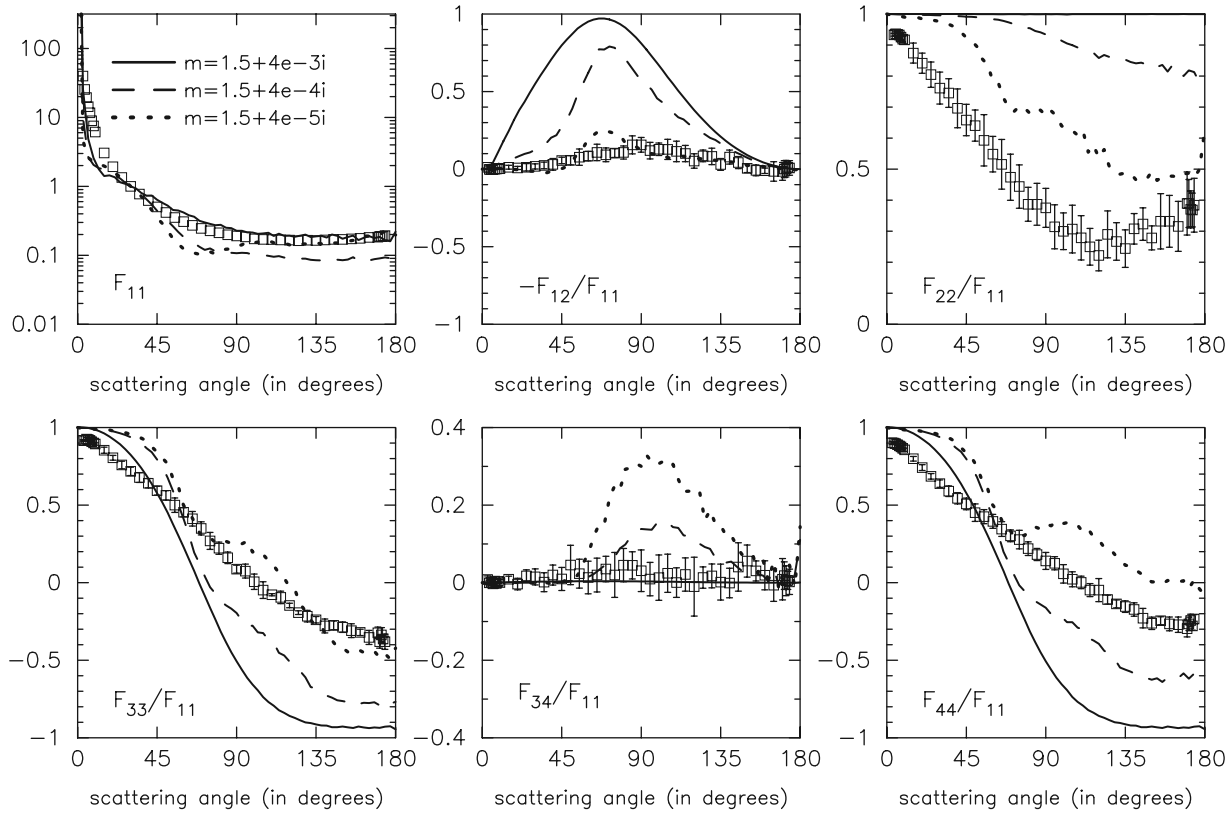

Figure 10. Scattering matrix elements computed with the traditional ray-optics method. The imaginary part of the refractive index, k is varied from 4E-3 to 4E-5. Further, we used $l_{min} = 2$, $\sigma = 0.2$, and the real part of the refractive index, n, equal to 1.5. The calculations are presented together with the experimental scattering matrix for Libyan sand at 632.8 nm (squares). Errors are indicated by error bars or are within the symbols.

model particles. For the power law covariance function applied, the minimum degree of the expansion, l_{min}, equals two or larger (the value of two corresponds to shapes obtained from the shape analysis, whereas a larger value can be given to increase the spikiness of the shapes). For the maximum degree of the expansion, l_{max}, we used a value of 25, which seems to be sufficiently large for our model shapes (see section 3.2). The particle size, specified by the mean radius R is randomly obtained from the particle size distribution for each model particle. Example images of particle shapes generated using the power law covariance function with varying l_{min} are shown in Figure 8. The number of triangles used to depict shapes in Figure 8 is identical to that used in scattering computations.

6.2. Model Computations

6.2.1. Traditional ROA Computations

[43] The model simulations were performed at a wavelength of 632.8 nm corresponding to the wavelength used in the light scattering experiments. The angular resolution of scattering was set to 3°, a compromise between precision and statistical noise. The same resolution was used both for the geometric optics and diffraction parts, although the forward diffraction peak was additionally calculated with much higher resolution in case it would be needed. The size distribution in the simulations was based on the fitted trimodal size distribution given in section 3.1. Furthermore, the shape parameters ν, σ, l_{min}, and l_{max} were fixed to 3.3, 0.2, 2, and 25, respectively (see sections 3.2 and 6.1). We used 1000 rays per shape and 1000 shapes per simulation, totaling a million rays per simulation that assured sufficient accuracy. However, some statistical noise remains in the resulting matrix elements. In particular at backward scattering angles the noise is apparently appreciable, as deduced from the violation of the general equalities (see equation (11)). This noise is due to the fact that few rays are scattered in backward directions. We investigated the reliability of the calculations by applying the Cloude (coherency matrix) test [*Hovenier and van der Mee*, 2000]. For all studied calculations the test was fulfilled at all scattering angles.

[44] In a first step we investigated the sensitivity of the scattering matrices of ensembles of Gaussian random particles by systematically varying the real and imaginary parts of the refractive index, n, and k, and the value of l_{min}. For the calculations we chose the following parameter values: $n = 1.3–1.6$ (in steps of 0.1), $k = 4 \cdot 10^{-5}–4 \cdot 10^{-3}$ (in steps of a factor of 10), and $l_{min} = 2–10$ (in steps of 1).

[45] In Figures 9–11 we present the calculated scattering matrices as functions of the scattering angle for various combinations of n, k, and l_{min}. All computed scattering matrices are presented together with the experimental data for the Libyan sand sample. For comparison with the experimental data all calculated phase functions are normalized to 1 at 30°. For simplicity, we only present some

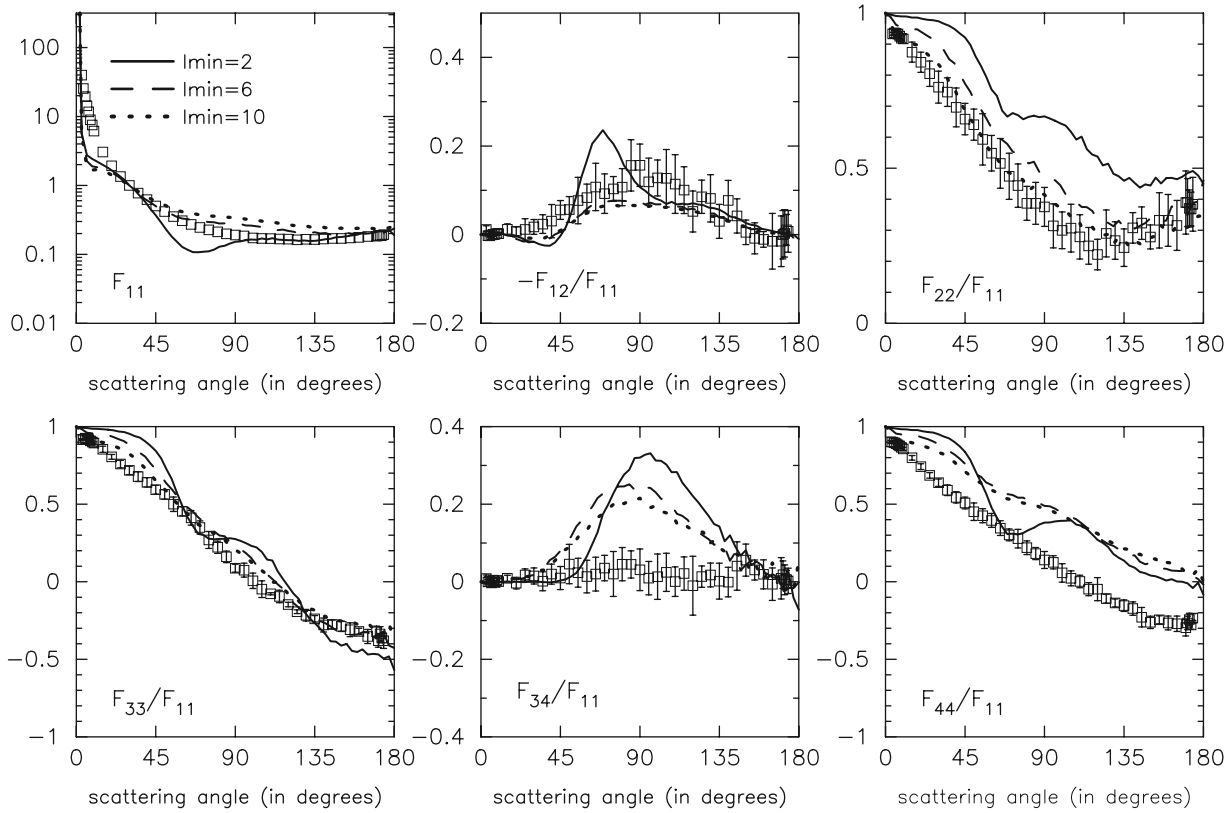

Figure 11. Scattering matrix elements computed with the traditional ray-optics method for $l_{min} = 2$ (solid), $l_{min} = 6$ (dashed), and $l_{min} = 10$ (dotted). The refractive index was fixed to $m = 1.5 + 4e - 5i$, and $\sigma = 0.2$. The calculations are presented together with the experimental scattering matrix for Libyan sand at 632.8 nm (squares). Errors are indicated by error bars or are within the symbols.

selected results that show the general effect of the model parameters on the scattering matrix elements.

[46] The results of varying the value of n on the calculated scattering matrix elements are presented in Figure 9. The imaginary part of the refractive index, k, was fixed to the estimated value for the Libyan sand sample, $k = 4 \cdot 10^{-3}$. We found very little effect when n is varied from 1.3 to 1.7. Specially the $F_{22}(\theta)/F_{11}(\theta)$ and $F_{34}(\theta)/F_{11}(\theta)$ are not affected at all by the changes in the real part of the refractive index.

[47] The effects of varying the imaginary part of the refractive index are shown in Figure 10. The steepness and shape of the $F_{11}(\theta)$ were significantly affected by the value of k. The maximum of the $-F_{12}(\theta)/F_{11}(\theta)$ strongly decreases when decreasing the value of k from $4 \cdot 10^{-3}$ to $4 \cdot 10^{-5}$. In contrast, the maximum of $F_{34}(\theta)/F_{11}(\theta)$ is affected in the opposite direction, i.e., it increases when decreasing the value of k. In general the calculated values of $-F_{12}(\theta)/F_{11}(\theta)$, $F_{22}(\theta)/F_{11}(\theta)$, $F_{33}(\theta)/F_{11}(\theta)$, and $F_{44}(\theta)/F_{11}(\theta)$ get closer to the measured values for small values of the imaginary part of the refractive index.

[48] According to these simulations we cannot obtain reasonably good fits by assuming the values for the refractive index presented in section 3.3, i.e., $m \simeq 1.5 + 4 \cdot 10^{-3}i$. As mentioned, a lower value of the imaginary part of the refractive index, k, would produce a better fit for almost all elements of the scattering matrix. Therefore we assume $m = 1.5 + 4 \cdot 10^{-5}i$ as the first guess for the ROA calculations. Even then, though, we could not obtain a good agreement between measured and calculated values by using realistic particle shapes. The combination of parameters that produces the best fit for realistic particle shapes without applying the Lambertian scheme is presented in Table 2, simulation set 1.

[49] It is known from previous studies [*Volten et al.*, 2001; *Nousiainen et al.*, 2003] that unrealistically spiky particle shapes ($l_{min} \sim 10$) can provide good fits. Therefore we also studied the effect of enhancing the roughness of the particles by using higher values of l_{min}. In Figure 11, we present the effect of different values of l_{min} on the calculated scattering matrix elements. As shown, a higher value of l_{min} produces a better fit for almost all elements of the scattering matrix, suggesting that the model particles based on the shape analysis are too smooth and do not scatter light diffusively enough. The increase of l_{min} decreases $-F_{12}/F_{11}(\theta)$ and $F_{22}(\theta)/F_{11}(\theta)$ at almost all scattering angles. It also decreases the value of $F_{33}(\theta)/F_{11}(\theta)$, and $F_{44}(\theta)/F_{11}(\theta)$

Table 2. Best Fit Parameters for Simulations Shown in Figure 14

Simulation Set	n	k	l_{min}	f_{ex}	α_{ex}	δ_{in}, μm	α_{in}	a
1	1.5	4e-5	2	-	-	-	-	0.86
2	1.5	4e-5	10	-	-	-	-	0.91
3	1.5	4e-4	2	0.08	0.25	500	0.25	0.63
4	1.5	4e-4	10	0.08	0.25	-	-	0.66

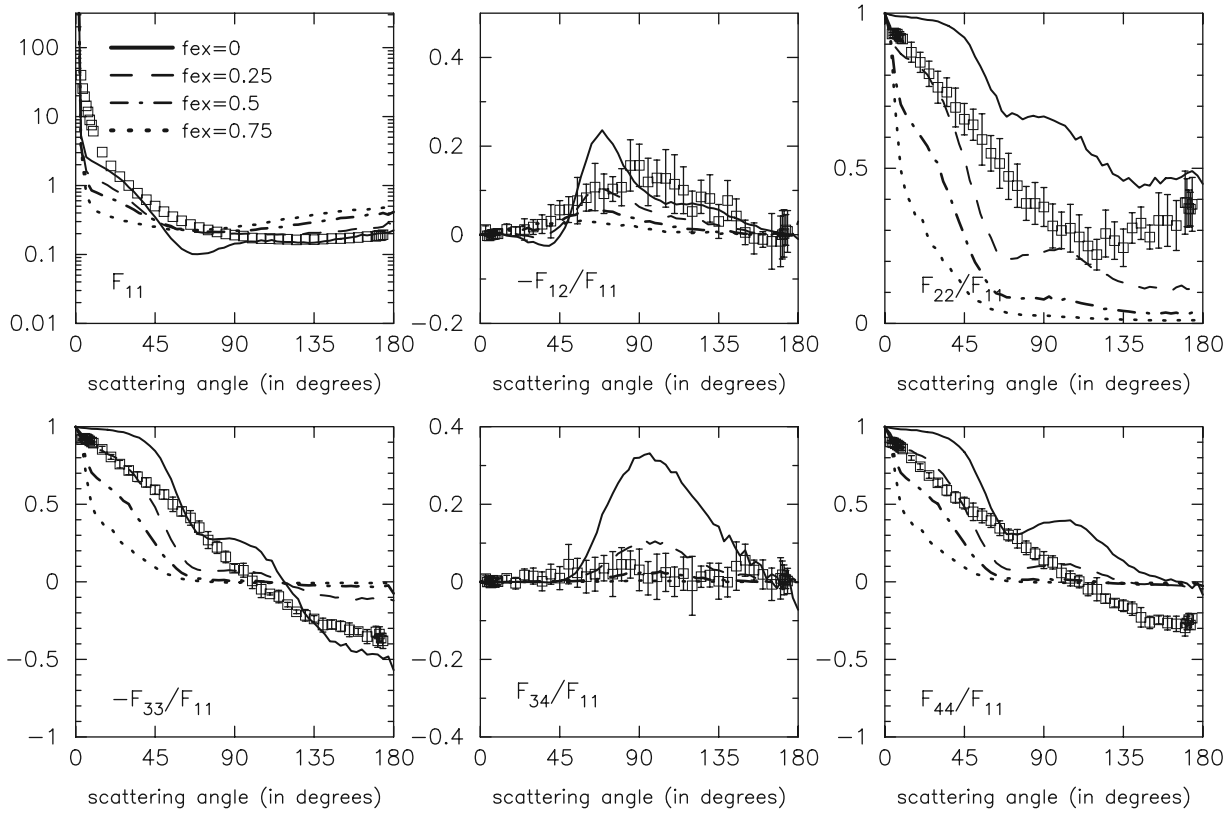

Figure 12. Effect of f_{ex} on the scattering matrix. The curves present the cases $f_{ex} = 0$ (solid), $f_{ex} = 0.25$ (dashed), $f_{ex} = 0.5$ (dotted-dashed), and $f_{ex} = 0.75$ (dotted), for $\alpha_{ex} = 0.5$ and internal Lambertian screens are excluded. The refractive index was fixed to $m = 1.5 + 4e - 5i$. The calculations are presented together with the experimental scattering matrix for Libyan sand at 632.8 nm (squares). Errors are indicated by error bars or are within the symbols.

at forward scattering angles. The best fit parameters correspond to simulation set 2 in Table 2.

6.2.2. Lambertian Simulations

[50] To improve the agreement with the measurements, we applied the Lambertian schemes. Firstly, we studied the dependence of the scattering matrix on the different Lambertian parameters, i.e., f_{ex}, α_{ex}, δ_{in}, and α_{in}. The sensitivity tests were performed for the retrieved shape and size parameters of our Libyan sand sample (see sections 3.1 and 3.2). Again all studied cases fulfilled the Cloude (coherency matrix) test at all scattering angles. The refractive index has been fixed to $m = 1.5 + 4 \cdot 10^{-5}$. For the calculations we chose the following combinations of Lambertian parameters: (1) For $\alpha_{ex} = 0.5$, the value of f_{ex} was varied from 0.1 to 1.0 in steps of 0.1. (2) For $f_{ex} = 0.2$, the value of α_{ex} was varied from 0.25 to 1.0 in steps of 0.25. (3) For $\alpha_{in} = 0.5$, δ_{in} took the following values: 500 μm, 250 μm, 100 μm, 50 μm, and 25 μm. (4) For $\delta_{in} = 500$ μm, the value of α_{in} was varied from 0.25 to 1.0 in steps of 0.25.

[51] In Figure 12, we present a selected set of computations that shows the effect of the value of f_{ex} on the scattering matrix elements. $F_{11}(\theta)$ increases at side and back scattering directions for increasing values of f_{ex}. In contrast an increase of f_{ex} decreases the calculated $-F_{12}(\theta)/F_{11}(\theta)$ at almost all scattering angles. In the same way, the maximum of $F_{34}(\theta)$ is strongly decreased when increasing the probability of Lambertian surface reflections and refractions. Moreover, an increase of f_{ex} affects the shape of $F_{22}(\theta)/F_{11}(\theta)$, decreasing its values at almost all scattering angles. The calculated values for the $F_{33}(\theta)/F_{11}(\theta)$, and $F_{44}(\theta)/F_{11}(\theta)$ also decrease in the forward scattering hemisphere when increasing the value of f_{ex}.

[52] The effect of varying α_{ex} is not shown here. Overall, the studied values of α_{ex} hardly affect $-F_{12}(\theta)/F_{11}(\theta)$ and $F_{34}(\theta)/F_{11}(\theta)$. However, high values of α_{ex} tend to keep $F_{22}(\theta)/F_{11}(\theta)$, $F_{33}(\theta)/F_{11}(\theta)$, and $F_{44}(\theta)/F_{11}(\theta)$ close to one at forward angles.

[53] Figure 13 shows the overall results of varying the mean free path length, δ_{in}, for the scattering matrix elements. The inclusion of internal screens seems to affect the scattering matrix in a way similar to that of the Lambertian surface elements. If the mean free path length is decreased the probability of an internal ray hitting a randomly oriented Lambertian screen is increased and $F_{11}(\theta)$ increases at almost all scattering angles. The effect of varying δ_{in} is substantial for the $F_{22}(\theta)/F_{11}(\theta)$, $F_{33}(\theta)/F_{11}(\theta)$, and $F_{44}(\theta)/F_{11}(\theta)$. The $F_{22}(\theta)/F_{11}(\theta)$ strongly decreases when δ_{in} is decreased at all scattering angles affecting also the shapes of the $F_{33}(\theta)/F_{11}(\theta)$, and $F_{44}(\theta)/F_{11}(\theta)$. The maximum of the $F_{34}(\theta)/F_{11}(\theta)$ is dramatically decreased for small values of δ_{in}. The parameter α_{in} has a very weak effect in the studied cases. Overall, the agreement between calculated and measured results is improved for smaller values of f_{ex} and α_{ex} and higher values of δ_{in}.

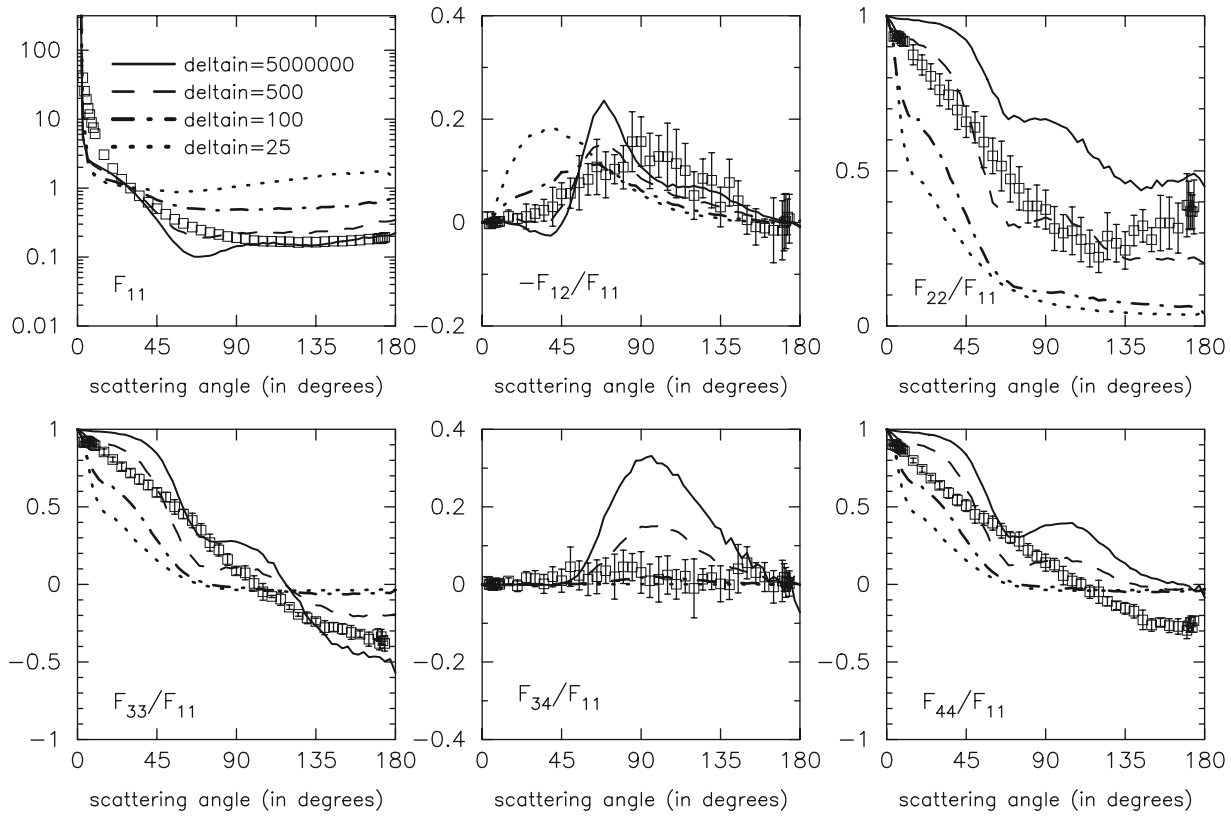

Figure 13. Effect of δ_{in} on the scattering matrix. The curves present the cases δ_{in} = 5000000 μm (solid), δ_{in} = 500 μm (dashed), δ_{in} = 100 μm (dotted-dashed), and δ_{in} = 25 μm (dotted), for α_{in} = 0.5 when surface Lambertian elements are excluded. The refractive index was fixed to $m = 1.5 + 4e - 5i$. The calculations are presented together with the experimental scattering matrix for Libyan sand at 632.8 nm (squares). Errors are indicated by error bars or are within the symbols.

[54] Once we knew the overall effects of the Lambertian parameters on the scattering matrix elements we performed further calculations in a narrower range of values for the Lambertian parameters. The value of f_{ex} was then varied from 0.06 to 0.2 in steps of 0.02. Additionally, the results of fixing δ_{in} at 500 μm and 250 μm was studied for different values of α_{in}. After the best fit Lambertian parameters were found we studied a possible best agreement between measured and calculated results by changing the values of the real and imaginary parts of the refractive index. The best fits were obtained for $m = 1.5 + 4 \cdot 10^{-4}i$. The best combination of input parameters is presented in Table 2, simulation set 3. Still, even by combining internal and external Lambertian reflections we cannot obtain reasonably good fits to all the experimental matrix ratios by assuming realistic shapes for the Libyan sand particles.

[55] Table 2 also presents the retrieved single-scattering albedos (a) for each simulation set. We might note that the calculated single scattering albedos are affected by the uncertainties of the albedo of the surface Lambertian elements, which is a free parameter, and of the unknown imaginary part of the refractive index.

[56] By checking all test simulations it turned out that very spiky shapes of the particles (l_{min} = 10) combined with a bit of Lambertian surface elements would produce reasonably good fits to the measurements (simulation set 4). The best fit cases for simulation sets 1, 2, 3, and 4 are presented in Figure 14.

7. Summary and Conclusions

[57] In this work we present measurements of the complete scattering matrix at 632.8 nm as a function of the scattering angle in the range 4 to 174° of a Sahara sand sample collected in Libya. The measured results follow the general trends presented by irregular mineral particles. To facilitate the use of the measured scattering matrix for multiple scattering calculations we also present a synthetic scattering matrix based on the measured scattering matrix covering the full angle range from 0 to 180°. The synthetic scattering matrix as a function of the scattering angle is presented in a table to facilitate the use of the data. The measured scattering matrices as well as the synthetic scattering matrix presented in this work are available at the Amsterdam Light Scattering Database (http://www.astro.uva.nl/scatter).

[58] The measured results for the Libyan sand sample were used to investigate whether the Ray Optics Approximation, ROA, can reproduce its scattering matrix as function of the scattering angle. The Libyan sand sample consists of quite large particles (r_{eff} = 124.75 μm) distributed over a narrow size distribution (v_{eff} = 0.15). Therefore it is an interesting test case for the Ray Optics Approxima-

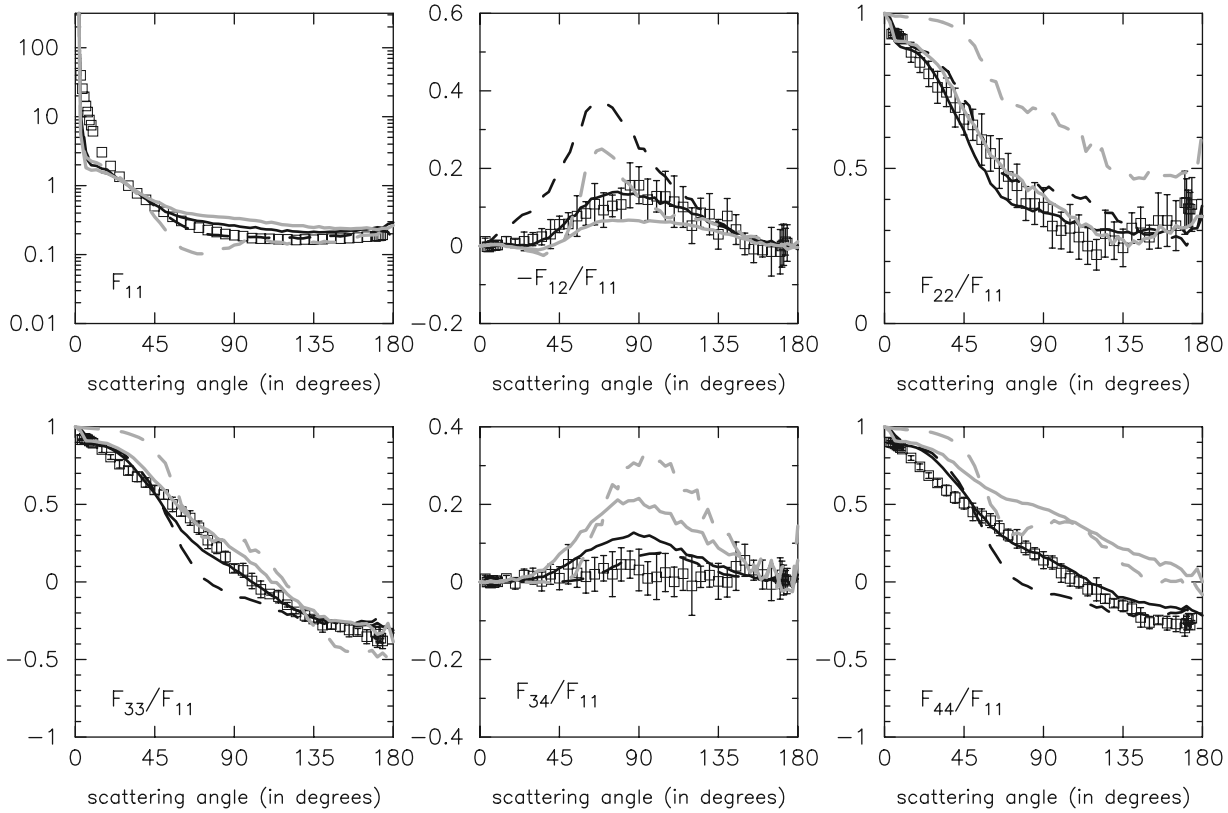

Figure 14. Comparison of the best fit cases for simulation set 1, (dashed grey line), simulation set 2 (solid grey line), simulation set 3 (dashed black line), and simulation set 4 (solid black line). The parameters for the corresponding simulations are shown in Table 2.

tion. Moreover, the ROA was also modified with ad hoc simple schemes of Lambertian surface elements and internal screens in order to reproduce the experimental data. The Lambertian external and internal schemes would simulate the small-scale surface roughness and internal structures, respectively. This method was successfully used in a previous work for another Sahara sand sample [*Nousiainen et al.*, 2003].

[59] Firstly, we analyzed our experimental results with the traditional ROA method by varying the real and imaginary parts of the refractive index. Model particle shapes were based on a shape analysis for the Libyan sand particles. We could not obtain simultaneous good fits for all scattering matrix elements by systematically changing the value of the real and imaginary parts of the refractive index for realistic shapes. Encouraged by the success obtained in previous simulations [*Volten et al.*, 2001; *Nousiainen et al.*, 2003], we tried to improve our fits by enhancing the surface roughness of the particles, i.e., increasing the value of $l_{\min}$. The assumption of unrealistically spiky particles improved the fits especially for $F_{11}(\theta)$ and $F_{22}(\theta)/F_{11}(\theta)$. Apparently, spikiness can actually mimic diffuse surface scattering.

[60] Secondly, we studied the effects of including the Lambertian surface elements to simulate diffuse surface scattering and the internal Lambertian screens to incorporate the effect of internal inhomogeneity. The ROA simulation with the best fit Lambertian parameters improves the agreement with the measurements for $F_{11}(\theta)$, $F_{22}(\theta)/F_{11}(\theta)$, and $F_{34}(\theta)/F_{11}(\theta)$. The improvement required, however, the decrease of the value of k to $4 \cdot 10^{-5}$ from the first-guess value $4 \cdot 10^{-3}$. In any case even by including the Lambertian schemes, we could not get reasonably good fits for all elements of the scattering matrix as functions of the scattering angle. Further, we tried to improve the fits to the experimental data for the Libyan sand by assuming unrealistic spiky particles with the inclusion of Lambertian schemes. The increase of $l_{\min}$ up to 10 produces better fits for almost all elements of the scattering matrix. *Nousiainen et al.* [2003] obtained good agreement with the measurements on another Sahara sand sample included in the Amsterdam Light Scattering Database by assuming realistic shapes when the Lambertian schemes were applied. In that case, the r_{eff} and v_{eff} were equal to 8.2 μm and 4.0, respectively. Because of computational limitations, the size distribution had to be truncated so that particles smaller than 2 μm were not taken into account. Still, there was a relatively high contribution to the scattering by small particles. Apparently, the contribution of those small particles could mimic the scattering effects of the small-scale surface roughness. Another possibility could be that the surface roughness characteristics of the former Sahara sand sample are different from those of the Libyan sand sample. All our results clearly show that the single-scattering properties of the Libyan sand particles cannot be accurately modeled without accounting for the effects of surface roughness. Further, the study shows that to do that properly we need something different from the Lambertian elements. The recent studies of light scattering by wavelength-scale Gaussian random particles by *Muinonen et al.* [2007],

Nousiainen and Muinonen [2007], and *Zubko et al.* [2007], allow us to identify the key scattering mechanisms: various dipole-dipole interactions due to the wavelength-scale surface roughness. For a detailed study of the mechanisms for wavelength-scale spherical particles, we refer the reader to *Tyynelä et al.* [2007]. A study of a realistic implementation of the small-scale surface roughness in the ray optics approximation is under way.

[61] **Acknowledgments.** We are indebted to A.González and D. Porcel from the Scientific Instrumentation Center of the University of Granada who took the FESEM and Optical images of the sample, respectively. T. Nousiainen and K. Muinonen acknowledge the Academy of Finland (contracts 212979 and 206206, respectively) for its financial support. The work of O. Muñoz, D. Guirado, and F. Moreno was partially supported by the Spanish Ministerio de Educación y Ciencia under contracts AYA2004-03250 and ESP2003-00357.

References

Bohren, C. F., and D. R. Huffman (1983), *Absorption and Scattering of Light by Small Particles*, John Wiley, New York.

Chiapello, I., C. Moulin, and J. M. Prospero (2005), Understanding the long-term variability of African dust transport across the Atlantic as recorded in both Barbados surface concentrations and large-scale Total Ozone Mapping Spectrometer (TOMS) optical thickness, *J. Geophys. Res.*, *110*, D18S10, doi:10.1029/2004JD005132.

d'Almeida, G. A. (1987), On the variability of desert aerosol radiative characteristics, *J. Geophys. Res.*, *92*(D3), 3017–3026.

d'Almeida, G. A., and L. Schütz (1983), Number, mass, and volume distribution of aerosol and soils of the Sahara, *J. Clim. Appl. Meteorol.*, *22*, 233–243.

Draine, B. T., and P. J. Flatau (1994), Discrete-dipole approximation for scattering calculations, *J. Opt. Soc. Am.*, *A11*, 1491–1499.

Dubovik, O., B. N. Holben, T. F. Eck, A. Smirnov, Y. Kaufman, M. D. King, D. Tanré, and I. Slutsker (2001), Variability of absorption and optical properties of key aerosol types observed in worldwide locations, *J. Atmos. Sci.*, *59*, 590–680.

Dubovik, O., B. N. Holben, T. Lapyonok, A. Sinyuk, M. I. Mishchenko, P. Yang, and I. Slutsker (2002), Non-spherical aerosol retrieval method employing light scattering by spheroids, *Geophys. Res. Lett.*, *29*(10), 1415, doi:10.1029/2001GL014506.

Dubovik, O., et al. (2006), Application of spheroid models to account for aerosol particle nonsphericity in remote sensing of desert dust, *J. Geophys. Res.*, *111*, D11208, doi:10.1029/2005JD006619.

Falkovich, A. H., E. Ganor, Z. Levin, P. Formenti, and Y. Rudich (2001), Chemical and mineralogical analysis of individual mineral dust particles, *J. Geophys. Res.*, *106*, 18,029–18,036.

Hansen, J. E., and L. D. Travis (1974), Light scattering in planetary atmospheres, *Space Sci. Rev.*, *16*, 527–610.

Haywood, J. M., P. N. Francis, M. D. Glew, and J. P. Taylor (2001), Optical properties and direct radiative effect of Saharan dust outbreaks using aircraft data, *J. Geophys. Res.*, *106*, 18,417–18,430.

Herman, M., J.-L. Deuzé, A. Marchand, B. Roger, and P. Lallart (2005), Aerosol remote sensing from POLDER/ADEOS over the ocean: Improved retrieval using nonspherical particle model, *J. Geophys. Res.*, *110*, D10S02, doi:10.1029/2004JD004798.

Hovenier, J. W. (2000), Measuring scattering matrices of small particles at optical wavelengths, in *Light Scattering by Nonspherical Particles*, edited by M. I. Mishchenko, J. W. Hovenier, and L. D. Travis, pp. 355–365, Academic, San Diego, Calif.

Hovenier, J. W., and C. V. M. van der Mee (2000), Basic relationships for matrices describing scattering by small particles, in *Light Scattering by Nonspherical Particles*, edited by M. I. Mishchenko, J. W. Hovenier, and L. D. Travis, pp. 61–85, Academic, San Diego, Calif.

Hovenier, J. W., H. Volten, O. Muñoz, W. J. van der Zande, and L. B. F. M. Waters (2003), Laboratory studies of scattering matrices for randomly oriented particles: Potentials, problems, and perspectives, *J. Quant. Spectrosc. Radiat. Transfer*, *79–80*, 741–755.

Hovenier, J. W., C. V. M. van der Mee, and H. Domke (2004), *Transfer of Polarized Light in Planetary Atmospheres, Basic Concepts and Practical Methods*, Springer, New York.

Kalashnikova, O. V., and I. N. Sokolik (2004), Modeling the radiative properties of nonspherical soil-delivered mineral aerosols, *J. Quant. Spectrosc. Radiat. Transfer*, *87*, 137–166.

Koepke, P., M. Hess, I. Shultz, and E. P. Shettle (1997), Global aerosol data set, *Rep., 44*, Max Planck Inst. for Meteorol., Hamburg, Germany.

Konert, M., and J. Vandenberghe (1997), Comparison of laser grain size analysis with pipette and sieve analysis: A solution for the underestimation of the clay fraction, *Sedimentology*, *44*, 532–535.

Koren, I., E. Ganor, and J. H. Joseph (2001), On the relation between size and shape of desert dust aerosol, *J. Geophys. Res.*, *106*, 18,037–18,045.

Levin, Z., J. H. Joseph, and Y. Mekler (1980), Properties of Sharav (Khamsin) dust-comparison of optical of optical and direct sampling data, *J. Atmos. Sci.*, *37*, 882–891.

Li, X., H. Maring, D. Savoie, K. Voss, and J. M. Prospero (1996), Dominance of mineral dust in aerosol light scattering in the North Atlantic trade winds, *Nature*, *380*, 416–419.

Li-Jones, X., and J. M. Prospero (1998), Variations in the size distributions of non-sea-salt sulfate aerosol in the marine boundary layer at Barbados: Impact of African dust, *J. Geophys. Res.*, *103*, 16,073–16,084.

Liu, L., M. I. Mishchenko, J. W. Hovenier, H. Volten, and O. Muñoz (2003), Scattering matrix of quartz aerosols: Comparison and synthesis of laboratory and Lorenz-Mie results, *J. Quant. Spectrosc. Radiat. Transfer*, *79–80*, 911–920.

Mackowski, D. W., and M. I. Mishchenko (1996), Calculation of the T matrix and the scattering matrix for ensembles of spheres, *J. Opt. Soc. Am. A*, *13*, 2266–2278.

Mishchenko, M. I., L. D. Travis, and D. W. Mackowski (1996), T-matrix computations of light scattering by nonspherical particles: A review, *J. Quant. Spectrosc. Radiat. Transfer*, *55*, 535–575.

Mishchenko, M. I., L. D. Travis, R. A. Kahn, and R. A. West (1997), Modeling phase functions for dustlike tropospheric aerosols using a shape mixture of randomly oriented polydisperse spheroids, *J. Geophys. Res.*, *102*, 831–837.

Mishchenko, M. I., W. J. Wiscombre, J. W. Hovenier, and L. D. Travis (2000), Overview of scattering by nonspherical particles, in *Light Scattering by Nonspherical Particles*, edited by M. I. Mishchenko, J. W. Hovenier, and L. D. Travis, pp. 20–60, Academic, San Diego, Calif.

Mishchenko, M. I., L. D. Travis, and A. A. Lacis (2002), *Scattering, Absorption, and Emission of Light by Small Particles*, Cambridge Univ. Press, New York.

Muinonen, K. (2000a), Light scattering by axially symmetric Gaussian random particles, in *Light Scattering by Nonspherical Particles: Halifax Contributions*, edited by G. Videen, Q. Fu, and P. Chýlek, pp. 91–94, U. S. Army Res. Lab., Adelphi, Md.

Muinonen, K. (2000b), Light scattering by stochastically shaped particles, in *Light Scattering by Nonspherical Particles*, edited by M. I. Mishchenko, J. W. Hovenier, and L. D. Travis, pp. 323–352, Academic, San Diego, Calif.

Muinonen, K., and J. S. V. Lagerros (1998), Inversion of shape statistics for small solar system bodies, *Astron. Astrophys.*, *333*, 753–761.

Muinonen, K., T. Nousiainen, P. Fast, K. Lumme, and J. I. Peltoniemi (1996), Light scattering by Gaussian random particles: Ray optics approximation, *J. Quant. Spectrosc. Radiat. Transfer*, *55*, 577–601.

Muinonen, K., L. Lamberg, P. Fast, and K. Lumme (1997), Ray optics regime for Gaussian random spheres, *J. Quant. Spectrosc. Radiat. Transfer*, *57*, 197–205.

Muinonen, K., J. Piironen, Yu, G. Shkuratov, A. Ovcharenko, and B. E. Clark (2002), Asteroid photometric and polarimetric phase effects, in *Asteroids III*, edited by W. Bottke et al., pp. 123–138, Univ. of Ariz. Press, Tucson.

Muinonen, K., E. Zubko, J. Tyynelä, Y. G. Shkuratov, and G. Videen (2007), Light scattering by Gaussian random particles with discrete-dipole approximation, *J. Quant. Spectrosc. Radiat. Transfer*, *106*(1–3), 360–377.

Muñoz, O., H. Volten, J. F. de Haan, W. Vassen, and J. W. Hovenier (2000), Scattering matrices of olivine and Allende meteorite particles, *Astron. Astrophys.*, *360*, 777–788.

Muñoz, O., H. Volten, J. F. de Haan, W. Vassen, and J. W. Hovenier (2001), Experimental determination of scattering matrices of fly ash and clay particles at 442 and 633 nm, *J. Geophys. Res.*, *106*, 22,833–22,844.

Muñoz, O., H. Volten, J. F. de Haan, W. Vassen, and J. W. Hovenier (2002), Experimental determination of the phase function and degree of linear polarization of El Chichón and Pinatubo volcacni ashes, *J. Geophys. Res.*, *107*(D13), 4174, doi:10.1029/2001JD000983.

Muñoz, O., H. Volten, J. W. Hovenier, B. Veihelmann, W. J. van der Zande, L. B. F. M. Waters, and W. I. Rose (2004), Scattering matrices of volcanic ash particles of Mount St. Helens, Redoubt, and Mount Spurr Volcanoes, *J. Geophys. Res.*, *109*, D16201, doi:10.1029/2004JD004684.

Muñoz, O., H. Volten, J. W. Hovenier, M. Min, Y. G. Shkuratov, J. P. Jalava, W. J. van der Zande, and L. B. F. M. Waters (2006), Experimental and computational study of light scattering by irregular particles with extreme refractive indices: Hematite and rutile, *Astron. Astrophys.*, *446*, 525–535.

Nousiainen, T., and G. M. MacFarquhar (2004), Light scattering by quasi-spherical ice crystals, *J. Atmos. Sci.*, *61*(18), 2229–2248.

Nousiainen, T., and K. Muinonen (2007), Surface-roughness effects on single-scattering properties of wavelength-scale particles, *J. Quant. Spectrosc. Radiat. Transfer*, *106*(1–3), 389–397.

Nousiainen, T., K. Muinonen, and P. Räisänen (2003), Scattering of light by large Saharan dust particles in a modified ray optics approximation, *J. Geophys. Res.*, *108*(D1), 4025, doi:10.1029/2001JD001277.

Patterson, E. M., D. A. Gillete, and B. H. Stockton (1977), Complex index of refraction between 300 and 700 nm for Saharan aerosols, *J. Geophys. Res.*, *82*(C21), 3153–3160.

Prospero, J. M., and P. J. Lamb (2003), African droughts and dust transport to the Caribbean: Climate change implications, *Science*, *302*(5647), 1024–1027.

Shettle, E. P., and R. W. Fenn (1979), Models of aerosols of lower troposphere and the effect of humidity variations on their opticla properties, *AFCRL Tech. Rep. 79 0214*, Air Force Cambridge Res. Lab., Hanscom Air Force Base, Mass.

Tyynelä, J., G. Videen, and K. Muinonen (2007), Interrelatng angular scattering characteristics to internal electric fields for wavelength-scale spherical particles, *J. Quant. Spectrosc. Radiat. Transfer*, *106*(1–3), 520–534.

Van de Hulst, H. C. (1957), *Light Scattering by Small Particles*, John Wiley, New York.

Volten, H., O. Muñoz, E. Rol, J. F. de Haan, W. Vassen, J. W. Hovenier, K. Muinonen, and T. Nousiainen (2001), Scattering matrices of mineral aerosol particles at 441.6 nm and 632.8 nm, *J. Geophys. Res.*, *106*, 17,375–17,401.

Volten, H., O. Muñoz, J. W. Hovenier, J. F. de Haan, W. Vassen, W. J. van der Zande, and L. B. F. M. Waters (2005), WWW scattering matrix database for small mineral particles at 441.6 and 632.8 nm, *J. Quant. Spectrosc. Radiat. Transfer*, *90*(2), 191–206.

Volten, H., O. Muñoz, J. W. Hovenier, and L. B. F. M. Waters (2006), An update of the Amsterdam light scattering database, *J. Quant. Spectrosc. Radiat. Transfer*, *100*, 437–443.

Yang, P., and K. N. Liou (1996), Geometric-optics-integral-equation method for light scattering by nonspherical ice crystals, *Appl. Opt.*, *35*, 6568–6584.

Zubko, E., K. Muinonen, Y. G. Shkuratov, G. Videen, and T. Nousiainen (2007), Scattering of light by roughened Gaussian random particles, *J. Quant. Spectrosc. Radiat. Transfer*, *106*(1–3), 604–615.

D. Guirado, F. Moreno, and O. Muñoz, Instituto de Astrofísica de Andalucía, Consejo Superior de Investigaciones Científicas, Camino Bajo de Húetor 50, E-18008 Granada, Spain. (olga@iaa.es)

J. W. Hovenier and L. B. F. M. Waters, Astronomical Institute "Anton Pannekoek," University of Amsterdam, Kruislaan 403, NL-1098 SJ Amsterdam, Netherlands.

K. Muinonen, Observatory, University of Helsinki, P.O. Box 14, FIN-00014 Helsinki, Finland.

T. Nousiainen, Department of Physical Sciences, University of Helsinki, P.O. Box 68, FIN-00014 Helsinki, Finland.

H. Volten, Laboratory for Environmental Monitoring, Environment and Safety Division, National Institute of Public Health and the Environment, Antonie van Leeuwenhoeklaan 9, NL-3721 MA Bilthoven, Netherlands.